LA-UR-20-26089
Approved for public release; distribution is unlimited.

Title: High Order Implicit Residual-Based Spatial Discretization Error Estimation for SN Neutron Transport

Author(s): Hart, Nathan Henry
Azmy, Yousry Y.

Intended for: Mark Mills Award (ANS)

Issued: 2020-08-10

High Order Implicit Residual-Based Spatial Discretization Error Estimation for S_N Neutron Transport

Nathan H Hart[a,1], Yousry Y Azmy[a]

[a] *North Carolina State University*
Department of Nuclear Engineering
2500 Stinson Drive, Raleigh, NC 27606

Abstract

This work demonstrates our novel residual source spatial discretization error estimator (LeR/TE-AD) for a DGFEM-1 discretization and assesses it along with two contemporary estimators, Ragusa and Wang's h-refinement estimator (RW) and Duo, Azmy, and Zikatanov's explicit residual-based estimator (DAZ), on a suite of Method of Manufactured Solutions (MMS) 2D problems and three realistic problem geometries. LeR/TE-AD is attractive because it directly estimates the local error in the angular flux, as opposed to a mere indicator of the error's behavior, on the same mesh and method order as the original numerical solution, thus typically being less computationally intensive than a refinement-based method. On the MMS suite, LeR/TE-AD consistently displayed a reduced performance versus its DGFEM-0 results in terms of accuracy and precision metrics, though it was not typically grossly inaccurate. This is attributed to the irregularities in the true solution across singular characteristics limiting the local accuracy of the numerical flux solution, leading to poor derivative approximations used in the residual approximations. The error transport problem then spreads the error in the residual to nearby cells, causing a greater degree of imprecision that did not afflict DAZ or RW.

In testing the estimators on realistic problem geometries, however, LeR/TE-AD fared better. In practice, the true error is much larger in non-idealized geometries like in MMS, and a superlinear true solution means that RW and DAZ are not beneficially biased for DGFEM-1 error estimation. LeR/TE-AD was typically first or second in accuracy, primarily competing with RW, but the latter usually consumed 2-4 times the computational time as LeR/TE-AD, and requires a solution with four times as many unknowns. Furthermore, RW and LeR/TE-AD can be used to compute direct estimates of the error in any quantity of interest that is based on the angular flux solution, such as the fission rate density in a fuel pin, whereas DAZ requires a heuristic extension due to its norm-based nature.

[1] Currently at Los Alamos National Laboratory, nhhart@lanl.gov

1. Introduction

The S_N form of the steady-state, one-speed particle transport equation typically requires a spatial discretization scheme in order to be solved. The solution to this discretized transport equation incurs error *vis-a-vis* the solution to the spatially undiscretized transport equation (the "true solution"). Since the latter is usually an unknown quantity, an estimate of the error is required for any error-driven scheme such as adaptive mesh refinement (AMR) ([1, 2, 3]) or error analysis ([4, 5]).

As the spatial discretization scheme is refined either in mesh size or method order, the discrete solution can better approximate the true solution where it is smooth. However, in multidimensional geometries, singular characteristics propagate from irregularities in the boundary conditions ([6]), as well as source discontinuities and material heterogeneities, across which the true solution is not infinitely differentiable, and they incur additional error in the solution if the order of irregularity is not sufficiently high as to be adequately captured by the truncated scheme. For the discontinuous Galerkin finite element method of order Λ ([7]), DGFEM-Λ, the effect of true solution irregularity order on the convergence of the global L_2 norm of the error has been determined to be

$$||\psi_h^\Lambda - \psi||_{L_2(\mathcal{D})} \leq Ch^{\min(\Lambda+1,r)}, \tag{1}$$

where ψ is the true angular flux solution, ψ_h^Λ is the solution to the discretized transport equation on an h-level mesh and with method order Λ, C is a constant independent of mesh size, $\mathcal{D}$ is the domain, and r is the true solution regularity order ([8, 9, 10]). This result demonstrates that, globally, irregularity can limit the accuracy of the numerical solution, and there comes a point where increasing Λ fails to improve accuracy by this metric. The true solution regularity order is represented by the Sobolev space in which the true solution belongs; in 2D, for continuous solutions, the space is at most $\psi \in H^{3/2-\nu}(\mathcal{D})$, and for discontinuous solutions, the space is at least $\psi \in H^{1/2-\nu}(\mathcal{D})$, where ν is very small and positive ([11, 10, 12]).

The above information is vital to understanding how error estimation may change with order refinement. *A posteriori* error estimation requires using the numerical solution to recover some truncated features of the true solution and either directly approximate the error or approximate a residual term to either solve an auxiliary partial differential equation or inform a bound on the global error in some norm ([13, 14, 15, 16, 17, 18]). Because solution convergence rate with mesh refinement is limited by regularity order, improved estimator performance with increasing method order is not necessarily expected. In Wang and Ragusa, [19], difference-based and projection-based h-refinement estimators appear to become more accurate in an absolute sense with increasing method order, but the jump-based error indicator exhibits no such improvement. Examining error estimators

over a set of Method of Manufactured Solutions (MMS) test problems in [20], O'Brien and Azmy demonstrate that Ragusa and Wang's difference-based h-refinement estimator ([21]) becomes more accurate in a relative sense as well with increasing method order. However, O'Brien and Azmy also demonstrate that, despite becoming more accurate in an absolute sense, a jump-based indicator and implicit finite element residual-based error estimator actually become less accurate in a relative sense with increasing method order ([20]). This is attributed to the failure of the basis space to capture singularities.

We have previously developed a novel implicit discrete residual-based error estimator named the "residual source estimator" and assessed it against Ragusa and Wang's h-refinement estimator and Duo, Azmy, and Zikatonov's explicit residual-based error bound ([22]) in [23, 24], finding it to be accurate and precise at a reduced computational cost to the h-refinement estimator for a DGFEM-0 method. However, it was found that the estimators exhibited generally worse performance, per a parameter-wide metric-based evaluation using MMS, when examined for discontinuous solutions. That is, the estimators were adversely affected when the limiting exponential in Eq. 1 was the regularity order. Hence, in increasing the method order to DGFEM-1, all problem configurations will have the regularity order setting the limiting exponential.

We are primarily interested in evaluating the residual source estimator on more state-of-the art methods, namely a piecewise linear DGFEM-1 method, and on realistic problem geometries, to demonstrate the advantages and disadvantages of using the method in practical applications. The work will proceed as follows. In Sec. 2 the relevant transport and error estimation methodology and residual source estimator will be detailed, and the required residual and derivative approximations for DGFEM-1 will be introduced. In Sec. 3.1 the residual source estimator and the two aforementioned estimators will be evaluated *via* an MMS case study. In Sec. 3.2 a parameter-wide metric-based evaluation, similar to [24], will be performed to reach general conclusions about estimator behavior with method order. In Sec. 4 the estimators will be evaluated on several realistic problem geometries with Richardson extrapolation-derived reference solutions for DGFEM-0 and DGFEM-1 discretizations to assess the generality of the conclusions obtained from the parameter-wide evaluations. Finally, conclusions will be given in Sec. 5.

2. Methodology

2.1. Terminology

The true solution is considered the solution to the one-speed, steady-state transport equation in 2D Cartesian geometry with a non-multiplying medium characterized by isotropic scattering,

$$\left(\mu_m \frac{\partial}{\partial x} + \eta_m \frac{\partial}{\partial y} + \sigma_t(x,y)\right)\psi_m(x,y) = \mathcal{S}\psi_m(x,y) + q(x,y), \\ m = 1,\ldots,M,\ (x,y) \in \mathcal{D}, \tag{2}$$

where M is the total number of discrete ordinates, σ_t and σ_s are the macroscopic total and scattering cross-sections, respectively, and

$$\mathcal{S}\psi_m(x,y) = \sigma_s(x,y)\sum_m^M w_m\psi_m(x,y) = \sigma_s(x,y)\phi(x,y), \tag{3}$$

is the isotropic scattering source. Standard notation applies otherwise ([25]). Though these simplifications incur their own error ([26, 27, 28]), standard practice is to consider the spatial discretization error as separable from other sources of error ([13, 16]). The explicit boundary conditions (BCs) are,

$$\psi_m(x,y) = \Psi_m(x,y),\ \forall\ \hat{n}\cdot\vec{\Omega}_m < 0,\ (x,y) \in \partial\mathcal{D}, \tag{4}$$

where $\partial\mathcal{D}$ is the boundary of the rectangular domain, $\mathcal{D} = (0,X)\times(0,Y)$. Equation 2 is rewritten in operator form,

$$L\psi = \mathcal{S}\psi + q, \tag{5}$$

with angle subscripts henceforth dropped for brevity, unless otherwise noted. Because the solution to Eqs. 2 and 4 cannot typically be computed analytically, the Method of Manufactured Solutions (MMS), as outlined in [29], is utilized in this work to acquire reference solutions against which the numerical solution's true error is computed. To keep the problems somewhat consistent across the MMS suite, dimensions of $\mathcal{D}$ are fixed at $X = Y = 1$ cm, and S_4 Level-Symmetric quadrature is exclusively used. All parameters are constant across the domain, and solutions are manipulated by adjusting three parameters: the optical thickness *via* σ_t, the scattering ratio $c = \sigma_s/\sigma_t$, and the solution regularity *via* the BCs.

The DGFEM-Λ scheme, detailed in [7, 30, 31], is used exclusively. The crux of the method is that the solution spatial dependency is represented within a cell, $K^{(i,j)} = (x_{i-1},x_i)\times(y_{j-1},y_j)$, as a series of smooth Legendre polynomials up to order Λ, with coefficients determined by solving the discretized transport equation, Eq. 6,

$$L_h^\Lambda\psi_h^\Lambda = \mathcal{S}\psi_h^\Lambda + \Pi_h^\Lambda q, \tag{6}$$

where L_h^Λ is the discretized transport operator, and Π_h^Λ is an L_2 projection operator onto the DGFEM-Λ test space and h-level mesh. BCs are obtained by L_2 projection of Eq. 4 onto the test space.

The spatial discretization error is then defined as the difference between the projected true solution and the numerical solution Eq. 7, and it exists in the same space as the numerical angular flux solution, i.e, it is an angular quantity represented by a series of Legendre polynomials within a cell.

$$\varepsilon_h^\Lambda \equiv \psi_h^\Lambda - \Pi_h^\Lambda \psi \tag{7}$$

Henceforth, an estimate of this quantity will be denoted ϵ_h^Λ. The error and error estimates are condensed into cell-wise L_2 norms, $E^{(i,j)}$ and $e^{(i,j)}$, respectively, and a local "effectivity index" is computed,

$$\theta^{(i,j)} \equiv \frac{e^{(i,j)}}{E^{(i,j)}} = \frac{\sqrt{\sum_m^M w_m \int_{K^{(i,j)}} dA\ (\epsilon_{h,m}^\Lambda)^2}}{\sqrt{\sum_m^M w_m \int_{K^{(i,j)}} dA\ (\varepsilon_{h,m}^\Lambda)^2}}. \tag{8}$$

A global effectivity index is likewise computed from global L_2 norms of the error, E, and error estimate, e,

$$\theta \equiv \frac{e}{E} = \frac{\sqrt{\sum_i^{N_x} \sum_j^{N_y} (e^{(i,j)})^2}}{\sqrt{\sum_i^{N_x} \sum_j^{N_y} (E^{(i,j)})^2}}. \tag{9}$$

This is a relative quantity, which means that even if the error converges in an absolute sense, i.e., $\lim_{h\to 0} e - E = 0$, it may not be "asymptotically exact" ([16]), i.e., $\lim_{h\to 0} \theta = 1$.

2.2. Residual Source Estimator

We have previously derived and demonstrated the residual source estimator for DGFEM-0 method in [23, 24], but a brief overview of the estimator follows here. Residual-based estimation can be explicit, that is, used to build a bound ([22, 32, 33]), or implicit, used to directly estimate the error via an auxiliary procedure ([17, 20, 34]). For the residual source estimator, the discrete residual, Eq. 10, is utilized, which represents the deviation in particle balance realized when the projected true solution is inserted into the discretized transport equation,

$$R_h^\Lambda \equiv \mathcal{S}\Pi_h^\Lambda \psi + \Pi_h^\Lambda q - L_h^\Lambda \Pi_h^\Lambda \psi. \tag{10}$$

Combining Eqs. 6, 7, and 10, and taking advantage of the linearity of the discretized transport operator, gives the error transport equation, Eq. 11,

$$L_h^\Lambda \varepsilon_h^\Lambda = \mathcal{S}\varepsilon_h^\Lambda + R_h^\Lambda, \tag{11}$$

where inflow error at the boundary is necessarily zero for explicit BCs, per Eq. 7. The solution to Eq. 11 is the true error provided the residual is computed exactly, but since the true solution is generally not known, the residual must be approximated.

2.3. DGFEM-1 Residual Approximation

To approximate the residual in a cell $K^{(i,j)}$, we use the Taylor expansion,

$$\begin{aligned}\psi(x,y) \approx \psi_{TE}^{(i,j)}(x,y) = \Bigg[\sum_{n_x=0}^{N} \sum_{n_y=0}^{N-n_x} \mathrm{sgn}(\mu)^{n_x} \mathrm{sgn}(\eta)^{n_y} \\ \times \frac{(x-x_o)^{n_x}(y-y_o)^{n_y}}{n_x! n_y!} \left[\frac{\partial^{n_x}}{\partial x^{n_x}} \frac{\partial^{n_y}}{\partial x^{n_y}} \psi \right]_{(x_o,y_o)_{K^{(i,j)}}} \Bigg],\end{aligned} \tag{12}$$

centered at

$$(x_o, y_o)_{K^{(i,j)}} = (x_{i-(1+\mathrm{sgn}(\mu))/2}, y_{j-(1+\mathrm{sgn}(\eta))/2}). \tag{13}$$

Then we project Eq. 12 onto the trial space to acquire the necessary true solution moments needed by Eq. 10. Thus, when considering the residual in a given cell $K^{(i,j)}$, the kl-moments of the true solution in cell $K^{(u,v)}$, denoted by $\psi_{kl}^{(u,v)}$, are approximated as

$$\psi_{kl}^{(u,v)} \approx \frac{1}{\Delta x_u \Delta y_v} \left(v_{k,l}^{(u,v)}, \psi_{TE}^{(i,j)}(x,y) \right), \tag{14}$$

where the two-dimensional inner product notation is used,

$$\left(f^{(u,v)}(x,y), g^{(i,j)}(x,y) \right) = \int_{x_{u-1}}^{x_u} dx \int_{y_{v-1}}^{y_v} dy \; f^{(u,v)}(x,y) g^{(i,j)}(x,y). \tag{15}$$

The cell dimensions are evaluated as $\Delta x_u = (x_u - x_{u-1})$ and $\Delta y_v = (y_v - y_{v-1})$. For DGFEM-$\Lambda$, the trial function $v_{k,l}^{(u,w)}$ belongs to the test space,

$$V(K^{(u,v)}) = \left\{ v_{k,l}^{(u,v)}(\tilde{x},\tilde{y}) = P_k(\tilde{x}_u) P_l(\tilde{y}_v) \mid \forall k,l = 0, ..., \Lambda \right\}, \tag{16}$$

where $P_k(\tilde{x}_u)$ is the k-order Legendre polynomial associated with the x-dimension, and analogously for $P_l(\tilde{y}_v)$ for the y-dimension. The variables

$$\tilde{x}_u = 2(x - x_{c,u})/\Delta x_u, \tag{17}$$

where $x_{c,u}$ is the x-coordinate of the cell midpoint, and analogously for $\tilde{y}$, are transformed spatial variables that allow for proper scaling of the Legendre polynomials' domain. The resultant approximated true solution in a cell $K^{(u,v)}$ for use in approximating the residual in that cell $K^{(i,j)}$ then takes the form

$$\Pi_h^{\Lambda} \psi \approx \sum_{k=0}^{\Lambda} \sum_{l=0}^{\Lambda} (2k+1)(2l+1) P_k(\tilde{x}_u) P_l(\tilde{y}_v) \psi_{kl}^{(u,v)}. \tag{18}$$

Equation 18 is evaluated for each cell $K^{(u,v)}$ that features in the expression of the residual in cell $K^{(i,j)}$[2], and the approximations are inserted into Eq. 10. Note that there are as many residual moments as there are solution moments. The resultant residual moment approximations for a given cell $K^{(i,j)}$ and direction of flight $\vec{\Omega}_m$, assuming constant material properties within a cell, for DGFEM-1 follow[3] in Eqs. 19-22:

$$\begin{aligned} R_{00}^{1,(i,j)} &= |\mu|(1-C_x^2)\frac{\Delta x_i}{12}\frac{\partial^2}{\partial x^2}\psi + |\eta|(1-C_y^2)\frac{\Delta y_j}{12}\frac{\partial^2}{\partial y^2}\psi \\ &\quad + \mathrm{sgn}(\eta)|\mu|(1-C_x^2)\frac{\Delta x_i \Delta y_j}{24}\frac{\partial^3}{\partial x^2 \partial y}\psi \\ &\quad + \mathrm{sgn}(\mu)|\eta|(1-C_y^2)\frac{\Delta x_i \Delta y_j}{24}\frac{\partial^3}{\partial x \partial y^2}\psi \\ &\quad + \frac{\Delta x_i^2}{12}\left(\frac{\partial^2}{\partial x^2}Q - \sigma_t^{(i,j)}\frac{\partial^2}{\partial x^2}\psi - \eta\frac{\partial^3}{\partial x^2 \partial y}\psi\right) \\ &\quad + \frac{\Delta y_j^2}{12}\left(\frac{\partial^2}{\partial y^2}Q - \sigma_t^{(i,j)}\frac{\partial^2}{\partial y^2}\psi - \mu\frac{\partial^3}{\partial x \partial y^2}\psi\right) + \mathcal{O}(\Delta^3), \end{aligned} \tag{19}$$

$$R_{10}^{1,(i,j)} = |\mu|(1+C_x^2)\frac{\Delta x_i}{12}\frac{\partial^2}{\partial x^2}\psi + \mathcal{O}(\Delta^2), \tag{20}$$

$$R_{01}^{1,(i,j)} = |\eta|(1+C_y^2)\frac{\Delta y_j}{12}\frac{\partial^2}{\partial y^2}\psi + \mathcal{O}(\Delta^2), \tag{21}$$

$$\begin{aligned} R_{11}^{1,(i,j)} &= \mathrm{sgn}(\mu)\mathrm{sgn}(\eta)\frac{\Delta x_i \Delta y_j}{36} \\ &\quad \times \left(\mu\frac{(1+C_x^2)}{2}\frac{\partial^3}{\partial x^2 \partial y}\psi + \eta\frac{(1+C_y^2)}{2}\frac{\partial^3}{\partial x \partial y^2}\psi\right) + \mathcal{O}(\Delta^3). \end{aligned} \tag{22}$$

Δ is a generic cell size term that assumes uniform refinement in the x- and y-dimensions. All derivatives are pointwise and evaluated at (x_o, y_o). The local mesh nonuniformity factors are

$$C_x = \frac{\Delta x_{i-\mathrm{sgn}(\mu)}}{\Delta x_i}, \tag{23}$$

and

$$C_y = \frac{\Delta y_{j-\mathrm{sgn}(\eta)}}{\Delta y_j}, \tag{24}$$

and $Q(x,y) = \mathcal{S}\psi(x,y) + q(x,y)$ is the combined scattering and fixed source. In order to evaluate these expressions for a cell that shares an inflow boundary with $\partial\mathcal{D}$, the appropriate nonuniformity factor(s) is set to 0. Because the Taylor expansion, Eq. 12, assumes sufficient solution regularity,

[2]In this work, the cells where this is necessary are $K^{(i,j)}$, $K^{(i-\mathrm{sgn}(\mu),j)}$, and $K^{(i,j-\mathrm{sgn}(\eta))}$. In the event that $K^{(i,j)}$ shares an inflow boundary with the domain boundary, the procedure is analogous, but with reduced dimensionality.

[3]More detailed discussions on the residual approximation and its derivation are found in [23, 24] for DGFEM-0 and in [35] for DGFEM-1.

the above expressions are invalid in cells intersected by SCs and their downwind first neighbors (by virtue of one of the necessary inflow moments requiring approximation). In practice, this is an accepted failing of the method, but the interested reader is referred to Chapter 6 in [35] for a discussion on this issue.

Note that all necessary pointwise derivatives evaluate to nil in the finite element representation of the solution. In fact, like in the case of DGFEM-0 ([24]), all derivatives one order higher than those captured by the DGFEM-Λ representation are required to approximate the residual. This signifies that, for sufficiently regular solutions, the DGFEM-1 residual is nil for true solutions that have a linear dependence in the spatial variables, meaning that the numerical solution is exact. Also like DGFEM-0 ([24]), the residual's 00-moment proportionality with Δ is dependent on the local uniformity of the mesh. Because the pointwise derivatives evaluate to nil in the finite element space, the derivatives must be approximated to elicit an *a posteriori* estimator.

The approximated residuals are henceforth denoted with $\mathcal{R}_h^\Lambda$ notation, and the residual source estimator with Taylor expansion-approximated residuals and approximated derivatives will be abbreviated as LeR/TE-AD.

2.4. DGFEM-1 Derivative Approximation

2.4.1. Patch Recovery Method

One method we have traditionally used for derivative approximation is an adaptation of the patch recovery method [15]. The true solution moments in the four cells that share a vertex with (x_o, y_o), Fig. 1 (or associated boundary surfaces, if $K^{(i,j)}$ shares an inflow boundary with $\partial\mathcal{D}$), are approximated using Eq. 14. This produces a system of equations that can be solved a couple different ways. One uses more solution moments to build the approximation, but theoretically gives a greater order of accuracy when the mesh is locally uniform. The other requires fewer solution moments to build the approximation, but maintains a reduced order of accuracy, even when the mesh is locally uniform. The approximated xx-derivative is

$$\begin{aligned}\frac{\partial^2}{\partial x^2}\psi = \frac{12C_y}{(1+C_x)(1+C_y)\Delta x_i^2}\Bigg(&\psi_{10}^{(i,j)} - \frac{1}{C_x}\psi_{10}^{(i-\mathrm{sgn}(\mu),j)} \\ &+\frac{1}{C_y}\psi_{10}^{(i,j-\mathrm{sgn}(\eta))} - \frac{1}{C_xC_y}\psi_{10}^{(i-\mathrm{sgn}(\mu),j-\mathrm{sgn}(\eta))}\Bigg) \\ &+ (C_x^2-1)\mathcal{O}(\Delta) + \mathcal{O}(\Delta^2),\end{aligned} \tag{25}$$

or by accepting a reduced order of accuracy in the particular case of a uniform mesh and using fewer moments,

$$\frac{\partial^2}{\partial x^2}\psi = \frac{12}{(1+C_x)\Delta x_i^2}\left(\psi_{10}^{(i,j)} - \frac{1}{C_x}\psi_{10}^{(i-\mathrm{sgn}(\mu),j)}\right) + \mathcal{O}(\Delta). \tag{26}$$

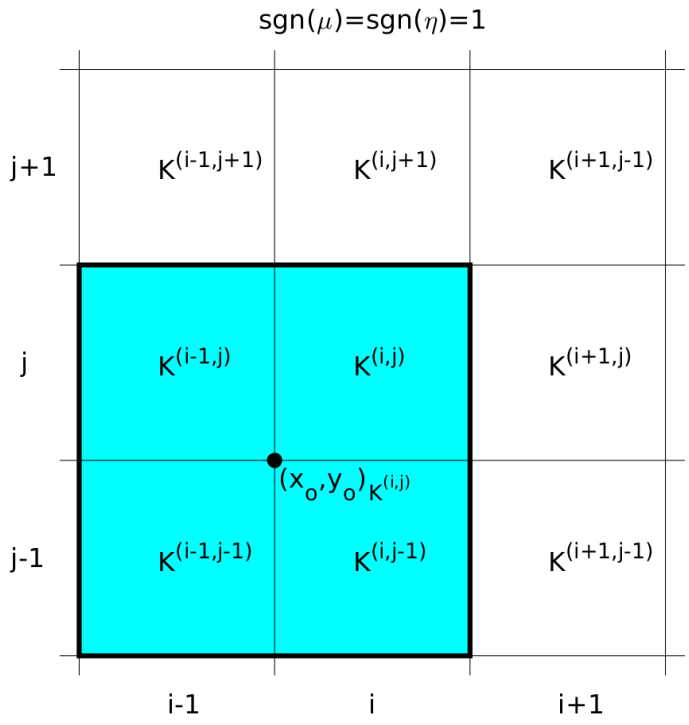

Figure 1: Example Patch of Cells for Angular Quadrant 1

The approximated yy-derivative can be found *via* rotation of Eqs. 25 and 26. The approximated xxy-derivative is

$$\frac{\partial^3}{\partial x^2 \partial y}\psi = \text{sgn}(\eta)\frac{36}{(1+C_x)\Delta x_i^2 \Delta y_j}\left(\psi_{11}^{(i,j)} - \frac{1}{C_x}\psi_{11}^{(i-\text{sgn}(\mu),j)} + \frac{1}{C_y}\psi_{11}^{(i,j-\text{sgn}(\eta))} - \frac{1}{C_x C_y}\psi_{11}^{(i-\text{sgn}(\mu),j-\text{sgn}(\eta))}\right) + (C_x^2 + C_y^2 - 2)\mathcal{O}(\Delta) + \mathcal{O}(\Delta^2), \tag{27}$$

or by accepting a reduced order of accuracy when the mesh is uniform and using fewer moments,

$$\frac{\partial^3}{\partial x^2 \partial y}\psi = \text{sgn}(\eta)\frac{72}{(1+C_x)\Delta x_i^2 \Delta y_j}\left(\psi_{11}^{(i,j)} - \frac{1}{C_x}\psi_{11}^{(i-\text{sgn}(\mu),j)}\right) + \mathcal{O}(\Delta). \tag{28}$$

The approximated xyy-derivative can also be found *via* rotation of Eqs. 27 and 28. The scalar flux derivatives are found by integrating the above equations, and the fixed source derivatives are considered known. The above equations are not valid on $\partial\mathcal{D}$, but the derivation of the applicable expressions for that case is done in an analogous manner, hence they are not included here for brevity, but the full set can be found in Chapter 3 of [35]. Two important points about Eqs. 25-28:

1) because Eq. 12 assumes sufficient regularity of the true solution, these equations are not valid when one of the cells in the patch is intersected by a SC. Furthermore, the order of accuracy of these methods assumes that the true solution moments are being used to recover the derivatives. In practice, the numerical solution may not be accurate enough to generate accurate derivative approximations.

In fact, this is found to be true when one of the local nonuniformity factors is not unity. It was noted in [24] that the derivative approximations on the boundary needed to be divided by a factor of two in order to converge to the correct value for DGFEM-0, and this is the case for DGFEM-1 also. However, it has been further determined that this is true for any local mesh nonuniformity; it was only previously apparent for the boundary cells because only uniform meshes were considered. Ultimately, this is a consequence of a failing in the DGFEM-Λ method, but it does not imply nonconvergence, as the solution still converges in an absolute sense; it is merely the derivative approximation that fails to converge in a relative sense.

2.4.2. Weak Derivative Recovery Method

To address the failing of the patch recovery method, we have developed an *ad hoc* derivative recovery method that is consistent with the DGFEM-Λ method termed the "weak derivative recovery method". This method acknowledges that the unknown derivatives do exist in the finite element space, albeit in their weak form. We start by applying Eq. 18 to the x-derivative of the angular flux,

$$\begin{aligned}\Pi_h^\Lambda \left[\frac{\partial}{\partial x}\psi\right]\Big|_{(x,y)} = &\left[\frac{\partial}{\partial x}\psi\right]_{00}^{(i,j)} + 3\left[\frac{\partial}{\partial x}\psi\right]_{10}^{(i,j)}\tilde{x} \\ &+ 3\left[\frac{\partial}{\partial x}\psi\right]_{01}^{(i,j)}\tilde{y} + 9\left[\frac{\partial}{\partial x}\psi\right]_{11}^{(i,j)}\tilde{x}\tilde{y}.\end{aligned} \tag{29}$$

Taking the x-derivative and evaluating at $\tilde{x} = \tilde{y} = -1$ (the transformed coordinates of (x_o, y_o)) gives

$$\frac{\partial}{\partial x}\,\Pi_h^\Lambda \left[\frac{\partial}{\partial x}\psi\right]\Big|_{(x_o,y_o)} = \frac{6}{\Delta x_i}\left[\frac{\partial}{\partial x}\psi\right]_{10}^{(i,j)} - \frac{18}{\Delta x_i}\left[\frac{\partial}{\partial x}\psi\right]_{11}^{(i,j)}. \tag{30}$$

Integrating by parts and applying the upwinding condition gives

$$\left[\frac{\partial}{\partial x}\psi\right]_{10}^{(i,j)} = \frac{3}{\Delta x_i}\left(\psi_{10}^{(i,j)} + \psi_{10}^{(i-\mathrm{sgn}(\mu),j)} - \frac{\psi_{00}^{(i,j)} - \psi_{00}^{(i-\mathrm{sgn}(\mu),j)}}{3}\right), \tag{31}$$

and

$$\left[\frac{\partial}{\partial x}\psi\right]_{11}^{(i,j)} = \frac{3}{\Delta x_i}\left(\psi_{11}^{(i,j)} + \psi_{11}^{(i-\mathrm{sgn}(\mu),j)} - \frac{\psi_{01}^{(i,j)} - \psi_{01}^{(i-\mathrm{sgn}(\mu),j)}}{3}\right). \tag{32}$$

Then, the resultant xx-derivative approximation for a cell not sharing an inflow boundary with $\partial\mathcal{D}$ is

$$\begin{aligned}\frac{\partial^2}{\partial x^2}\psi \approx \frac{\partial}{\partial x}\,\Pi_h^{\Lambda}\left[\frac{\partial}{\partial x}\psi\right]\Bigg|_{(x_o,y_o)} = \\ \frac{18}{\Delta x_i^2}\left(\psi_{10}^{(i,j)} + \psi_{10}^{(i-\mathrm{sgn}(\mu),j)} - \frac{\psi_{00}^{(i,j)} - \psi_{00}^{(i-\mathrm{sgn}(\mu),j)}}{3}\right) \\ + \frac{54}{\Delta x_i^2}\left(\psi_{11}^{(i,j)} + \psi_{11}^{(i-\mathrm{sgn}(\mu),j)} - \frac{\psi_{01}^{(i,j)} - \psi_{01}^{(i-\mathrm{sgn}(\mu),j)}}{3}\right).\end{aligned} \tag{33}$$

Taking the xy-derivative of Eq. 29 instead leads to the xxy-derivative for a cell not sharing an inflow boundary with $\partial\mathcal{D}$,

$$\begin{aligned}\frac{\partial^3}{\partial x^2\partial y}\psi \approx \frac{\partial^2}{\partial x\partial y}\,\Pi_h^{\Lambda}\left[\frac{\partial}{\partial x}\psi\right]\Bigg|_{(x_o,y_o)} = \\ \frac{108}{\Delta x_i^2\Delta y_j}\left(\psi_{11}^{(i,j)} + \psi_{11}^{(i-\mathrm{sgn}(\mu),j)} - \frac{\psi_{01}^{(i,j)} - \psi_{01}^{(i-\mathrm{sgn}(\mu),j)}}{3}\right).\end{aligned} \tag{34}$$

Approximations of the yy- and xyy-derivatives are found by rotation of Eqs. 33 and 34, respectively. The complete set of approximations, including those for cells that share inflow boundaries with $\partial\mathcal{D}$ can be found in [35], but are omitted here for brevity.

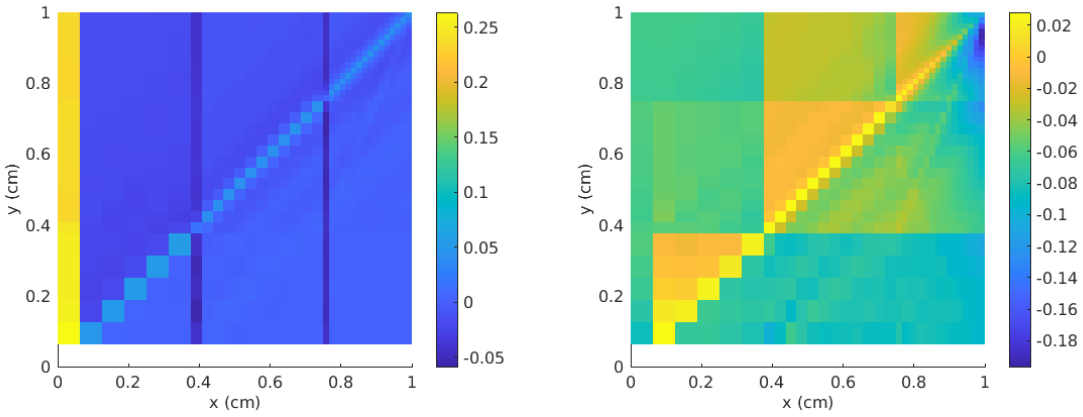

(a) Patch Recovery Method

(b) Weak Derivative Recovery Method

Figure 2: $\log_{10}$-Scale Ratio of Approximated to True xx-Derivatives for Single Ordinate

Figures 2 and 3 show the resultant relative error of the xx- and xxy-derivative approximations, respectively, on the $\mu = \eta = 0.35002$ ordinate for a nonuniform mesh for an MMS-generated problem where the true solution is irregular in its second derivative (to prevent nil derivatives and minimize SC-induced effects). The location of the nonuniformity-affected cells, including the boundary, is apparent in Fig. 2(a) as being the values that have the greatest error aside from the SC-intersected cells. The weak derivative method suffers no such penalty in these cells. However, the weak derivative

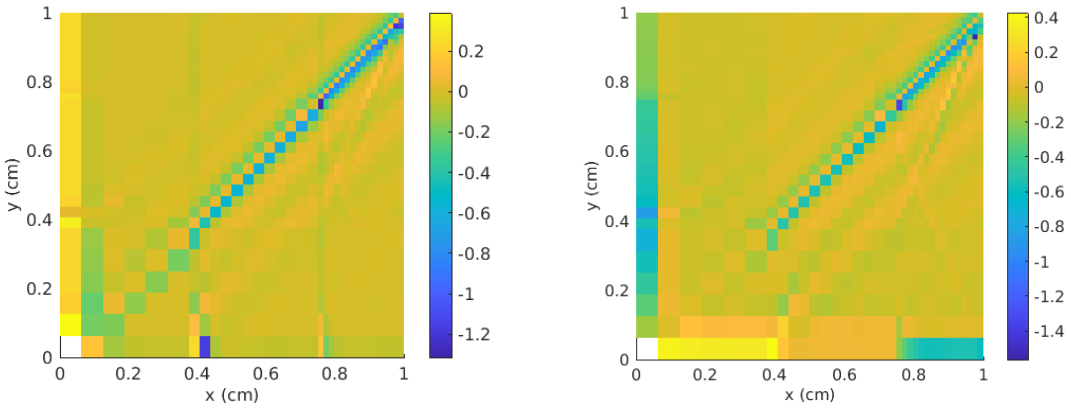

(a) Patch Recovery Method

(b) Weak Derivative Recovery Method

Figure 3: $\log_{10}$-Scale Ratio of Approximated to True xxy-Derivatives for Single Ordinate

recovery method appears to suffer on the inflow boundaries, but not other cells that abut cells of different size, for the high order cross derivative terms, Fig. 3(b).

Because nonuniformities are not present in this work, the patch recovery method with correction on the boundaries will continue to be used to keep consistent with previous work, but it is recommended that if the residual source estimator is to be implemented in any problem with numerous nonuniformities (e.g., AMR-generated meshes), the weak derivative method be used.

2.5. LeR/TE-AD Implementation

The error transport problem, Eq. 11, that is solved using the approximated residual as a fixed source is solved using the same code used to compute the initial numerical solution. In practice, little to no modification needs to be made to an existing transport code to perform this computation aside from removing likely restrictions on negative sources and solutions. For both transport computations, the source iteration method is employed with stopping criterion set to either an iterative error less than 10^{-10} or a max number of iterations of 500, whichever comes first, in order to produce an accurate scattering source.

LeR/TE-AD's computational process is summarized by the flowchart in Fig. 4. The inputs are the problem parameters, *viz.*, mesh parameters, solver inputs, and material properties, the numerical angular and scalar flux moments, and fixed source and BC derivatives, which are presumed known quantities. These quantities are used to approximate high-order derivatives required by Eqs. 19-22 and generate the error transport problem input. After the residual's approximated spatial distribution is computed, it is fed to the error transport problem routines with zero boundary conditions on $\partial\mathcal{D}$. After solving the error transport problem, the error is condensed into the local

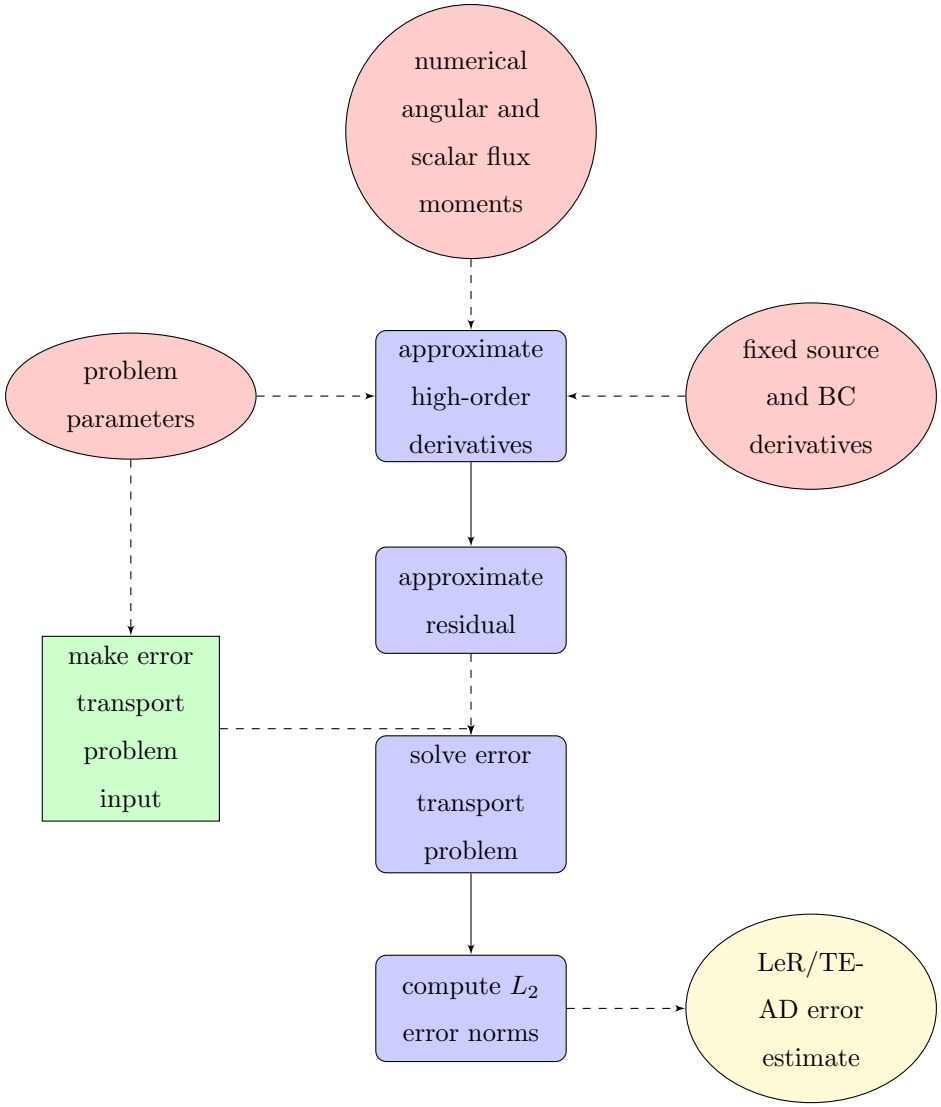

Figure 4: LeR/TE-AD Flow Chart

and global L_2 norms, which provide the sought error estimate.

3. MMS Evaluation

LeR/TE-AD is evaluated against two estimators, Ragusa and Wang's difference-based h-refinement estimator ([21]) with projected h-mesh solution preconditioning of the $h/2$-mesh solution (RW), and Duo, Azmy, and Zikatanov's explicit residual-based error bound ([22]) applied as a local indicator (DAZ). We implement the DAZ estimator by approximating the element residual and jump terms with a single-sweep of order DGFEM-$\Lambda+1$, preconditioned with the numerical DGFEM-Λ solution.

By focusing on MMS-generated solutions, we are able to observe the behavior of the estimators in idealized test conditions and attribute the effects of SCs to various features.

3.1. Case Study

Before examining LeR/TE-AD over the parameter space of the MMS suite, a case study is conducted to gain insight on estimator performance that will be generalized with metrics in the parametric evaluation. The MMS parameters for the case study follow: true solution irregular in the first derivative across SCs, total cross section $\sigma_t = 1.0$ cm^{-1}, and scattering ratio $c = 0.9$[4]. This problem is chosen because its angular flux solution is nonflat, and the magnitude of the irregularity is attenuated moderately by the transport processes in the host materials. The true scalar flux solution is plotted for a coarse (32×32) and fine (512×512) meshes in Fig. 8 below. The ratios

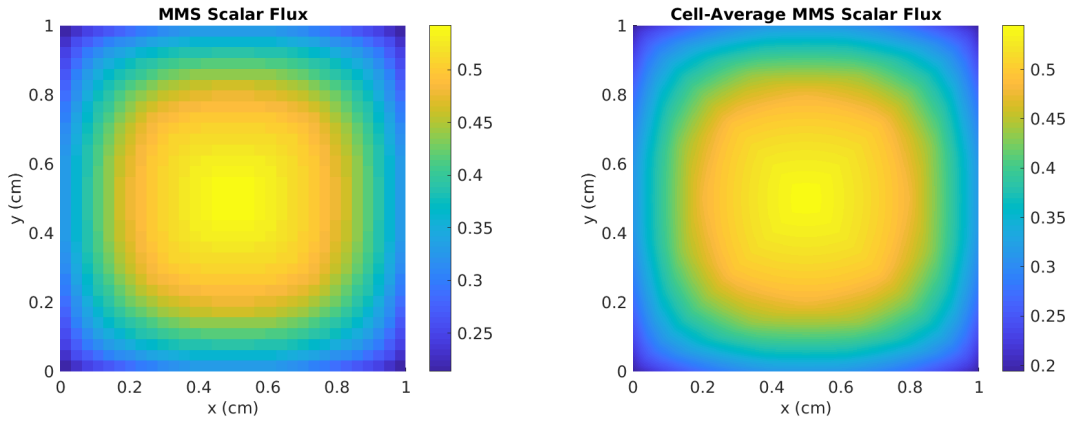

(a) Coarse Mesh

(b) Fine Mesh

Figure 5: Case Study: Cell-Averaged MMS Scalar Flux

of the resultant TE-AD residual moments approximations (derivatives approximated with corrected patch recovery) to the true residual moments are plotted over the domain in Fig. 6 on the coarse mesh for the ordinate $\mu = 0.35002$, $\eta = 0.86889$. Note that white space denotes that the denominator is zero due to the $\log_{10}$-scale applied to the ratio. Due to the MMS employed ([29]), all y-derivatives and cross derivatives are nil above the SC, and similarly all x-derivatives and cross derivatives are nil below the SC. Hence, per Eqs. 20-22, the true residual evaluates to zero in the corresponding regions. We notice that for the 00-moment, the residual in cells intersected by the SC associated with the ordinate are large outliers and tend to underapproximate the true residual. This is attributed to the noted failure of the Taylor expansion in the TE-AD residual approximation in the presence of

[4]This case is identical to that outlined in Section 5.1 in [24].

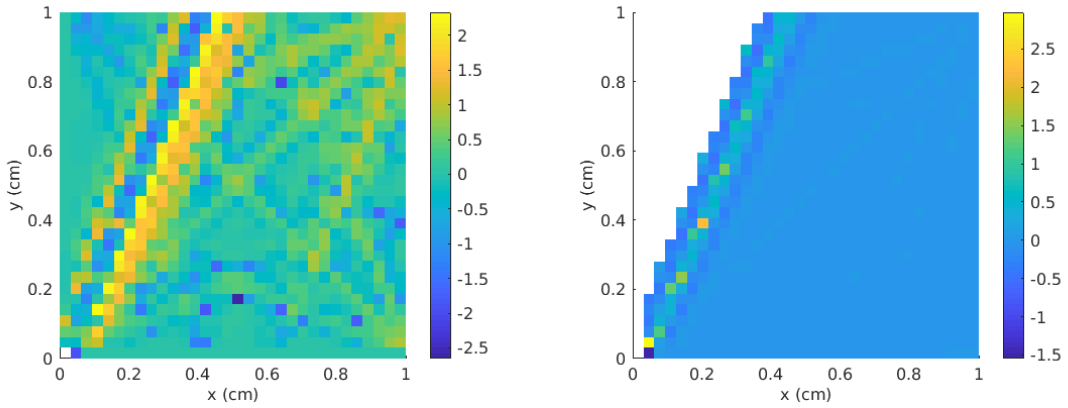

(a) $\log_{10}|\mathcal{R}^1_{00}/R^1_{00}|$

(b) $\log_{10}|\mathcal{R}^1_{01}/R^1_{01}|$

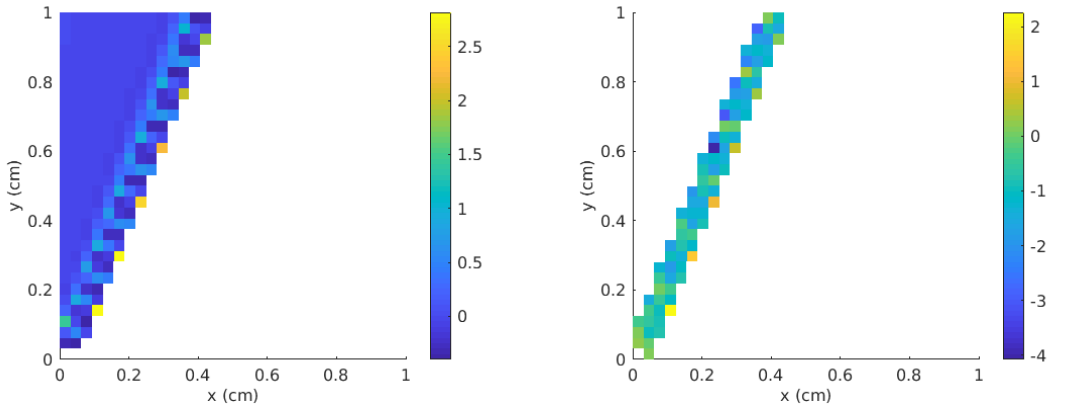

(c) $\log_{10}|\mathcal{R}^1_{10}/R^1_{10}|$

(d) $\log_{10}|\mathcal{R}^1_{11}/R^1_{11}|$

Figure 6: Case Study: Absolute Value of the Approximate/True Residual Moment Ratios, Coarse Mesh

irregularities. An additional "plume" of cells around the SCs also are large outliers, and they tend to overapproximate the true residual. In effect, the error in the streaming term resulting from the irregularity is numerically spread to nearby cells ([36]), making the numerical solution insufficiently accurate to acquire accurate derivative, and by extension residual, approximations. Some of the SCs belonging to other ordinates also appear due to the error in the scattering source incurred by the same effect. Apart from these localized effects, the residual generally is well approximated by the method. In examining the relative error of the 00-moment of the TE-AD residual on the fine mesh, Fig. 7, it is noted that as the measure of the set of cells traversed by the SCs decreases, the measure of the set of cells with high residual approximation error decreases, but the largest residual error magnitude increases greatly.

The resultant error estimates, plotted in Fig. 8, show that the estimator is quite consistent with the residual approximation. In cells surrounding SCs the error estimator is poor and oscillates

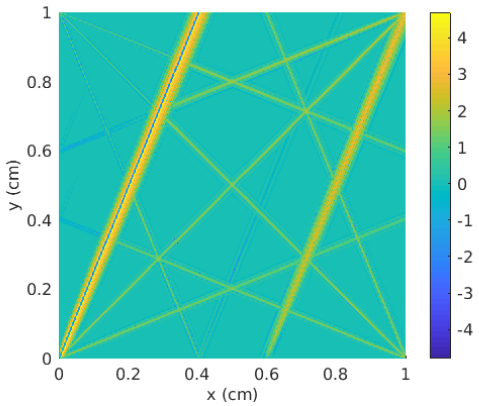

Figure 7: Case Study: $\log_{10}|\mathcal{R}^1_{00,n}/R^1_{00,n}|$, Fine Mesh
$\mu = 0.35002$, $\eta = 0.86889$

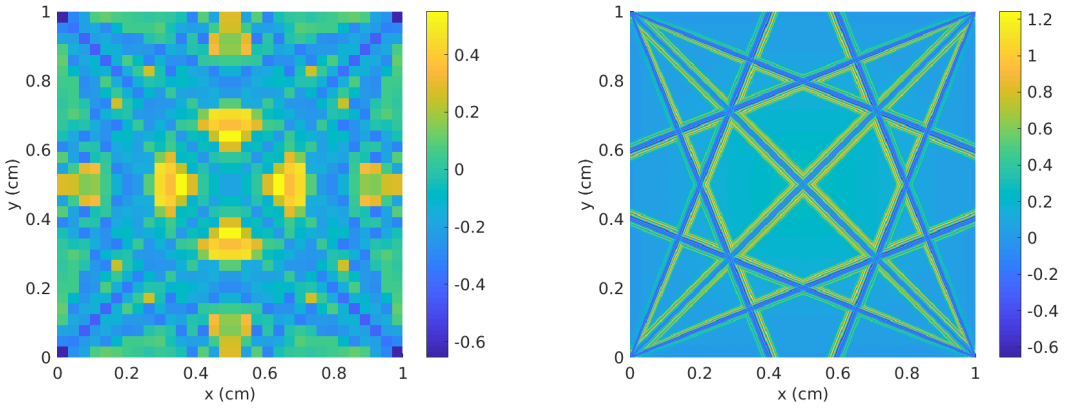

(a) Coarse Mesh

(b) Fine Mesh

Figure 8: Case Study: Local $\log_{10}$-Effectivity Index

about the true value, though the oscillation is due to oscillation in the true error near high gradient regions, per Godunov ([37]). Away from the SCs, however, the estimate appears to be accurate. The data plotted in Fig. 8(b) is recast as a histogram in Fig. 9, and shows that the estimator is accurate; i.e., there is a large peak centered near perfect agreement with the true error. However, the inaccuracies from the SCs manifest as long tails that extend in either direction. Furthermore, there is a small subpeak centered at slight overestimation of the true error. This is unlike the estimator for DGFEM-0 ([24]), and it is caused by accumulation of the error in the estimate from the residual approximation, spread by the error transport problem, in the center of the problem domain. Though the estimator suffers from the same effects for DGFEM-0, these are more influential for DGFEM-1 because the *relative* error in the residual approximation in the plume is greater. This is because

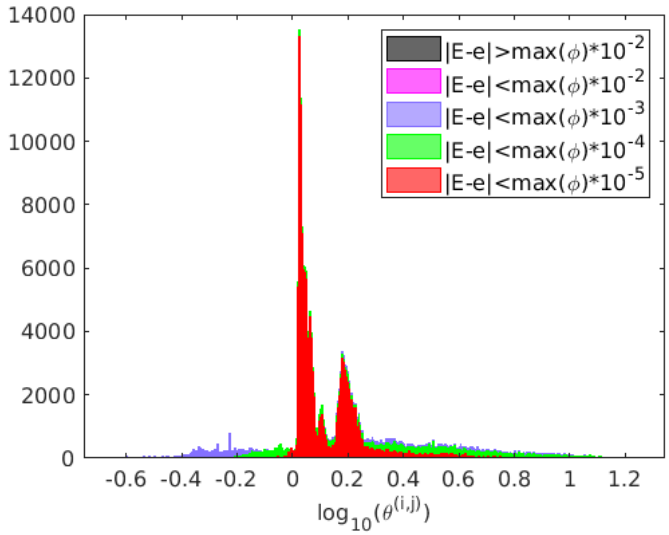

Figure 9: Case Study: LeR/TE-AD $\log_{10}$ Local Effectivity Index Histogram, Fine Mesh

the local convergence of the numerical solution is limited by true solution regularity in and near SC-intersected cells, the latter due to the numerical spread of error. Hence, the numerical solution locally maintains the same accuracy, but the residual goes to zero at a faster rate (than DGFEM-0), causing the residual approximation, which is constructed with the numerical solution, to have greater relative error *vis-a-vis* the DGFEM-0 residual approximation in the plume.

Finally, the color-coding of the histograms is related to the absolute error in the error estimate, scaled by the L_2 norm of the maximum scalar flux. In theory, if the absolute error is small and the relative error is large, this would signify that the true error is very nearly zero, and though the estimate cannot perfectly approximate its value, it is possibly "close enough" to zero to be considered a good estimate. This reduces the adverse implications of the subpeak in Fig. 9, since it is associated with a region with low absolute error in the error estimate.

The RW and DAZ estimator histograms for the same problem, Figs. 10 and 11, demonstrate that these estimators are highly precise; specifically, they exhibit tall and narrow peak heights. Additionally, RW is quite accurate. In both cases, the estimators' performance are superior to their performance for DGFEM-0 ([24]), unlike LeR/TE-AD. This is because LeR/TE-AD is unique in that it utilizes the error transport problem, which spreads locally-incurred inaccuracies near the SCs throughout the rest of the domain.

The absolute and relative convergence trends of the global error estimators are plotted in Fig. 12. The true residual is treated as an error indicator, i.e., Eq. 8 is computed with $\epsilon_h^\Lambda = R_h^\Lambda$, and analogously for the TE-AD residual as an error indicator using $\mathcal{R}_h^\Lambda$. The two estimators requiring auxiliary

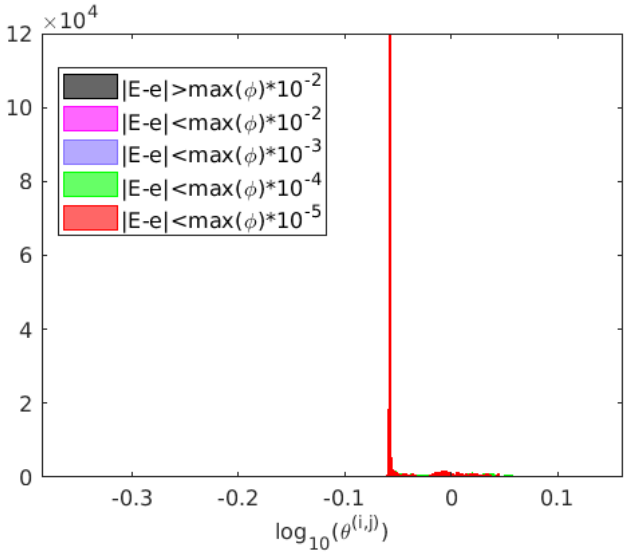

Figure 10: Case Study: RW $\log_{10}$ Local Effectivity Index Histogram, Fine Mesh

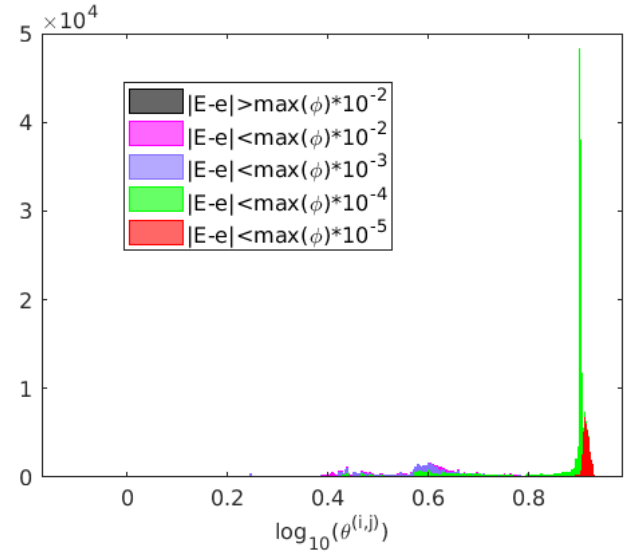

Figure 11: Case Study: DAZ $\log_{10}$ Local Effectivity Index Histogram, Fine Mesh

solutions, LeR/TE-AD and RW, are most accurate for this problem, though both underestimate the global error. Previously in [24], *ad hoc* analysis showed that h-refinement-based estimators will exhibit a propensity to underestimate the error and to not be asymptotically exact, and this is demonstrated in Fig. 12(b) for the RW h-refinement estimator, as its effectivity index does not approach 1 (0 in $\log_{10}$-scale) as $h^{-1} \to \infty$. However, LeR/TE-AD, which was not asymptotically exact for DGFEM-0, appears to be asymptotically exact for DGFEM-1 given this problem and set

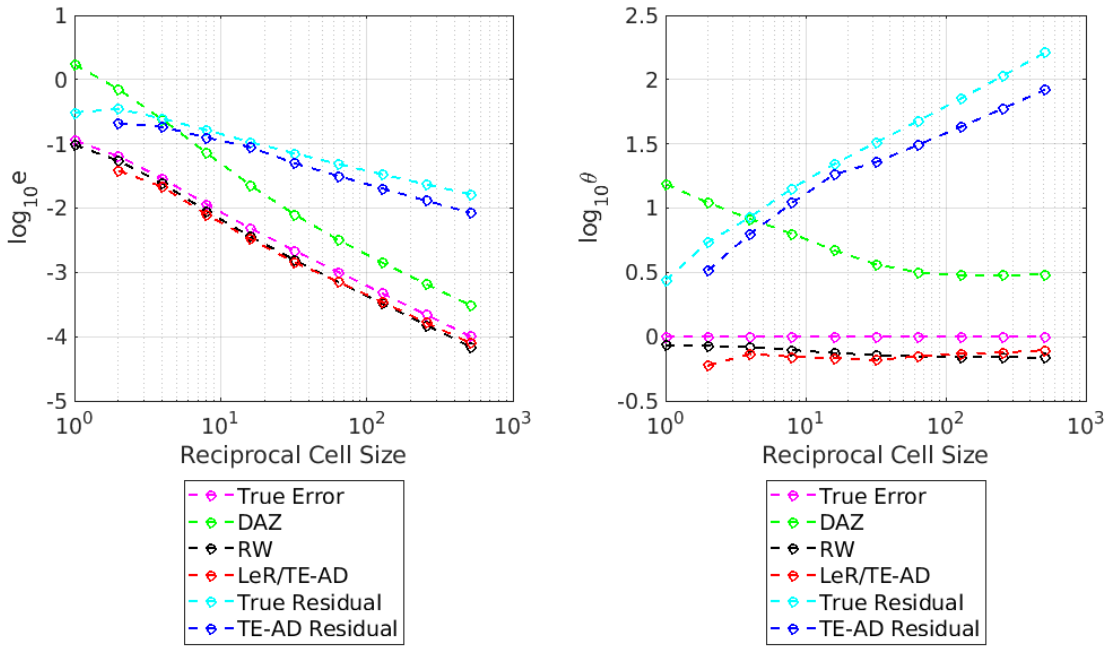

(a) Error Norm

(b) Effectivity Index

Figure 12: Case Study: Error Estimator Convergence with Mesh Refinement

of meshes, since its effectivity index is trending towards 1 for the last five meshes.

DAZ shows two different convergence rates, and these are attributed to the dominance of method truncation order, h^{Λ} at coarser meshes, by way of the element residual, and to the dominance of solution irregularity order, h^{r}, at finer meshes, by way of the jump terms. Finally, for DGFEM-Λ, it is not feasible to use the discrete residual alone as an error bound, as its L_2 norm does not converge at the same rate as the true error ([23]), as demonstrated for both the TE-AD and true residuals.

3.2. Metric-Based Evaluation

We have defined four metrics that are indicative of estimator performance: 1) the fraction of cells that have $\theta^{(i,j)} \geq 0$, an indicator of local boundedness, and useful for error analysis so long as the esitmate is not grossly inaccurate; 2) the fraction of cells that have $|\theta^{(i,j)} - 1| \leq \beta$, where β indicates a relative error in the error estimate and can be expressed as a percentage, an indicator of accuracy; 3) the standard deviation of $\log_{10} \theta^{(i,j)}$, an indicator of precision, useful for AMR applications; and 4) the additional computational cost incurred in computing the error estimate.

Along with the global effectivity index, these metrics are plotted over a range in MMS parameter space. Optical thickness, controlled by the total cross section, is examined over the range $\sigma_t =$

$[0.01, 0.1, 1.0, 10.0, 100.0]$. The scattering ratio range is $c = [0.1, 0.9]$. True solutions are either discontinuous or irregular in the first derivative across SCs. Furthermore, the mesh utilized is square and uniform in the range $N_x \times N_y = [32 \times 32, 512 \times 512]$.

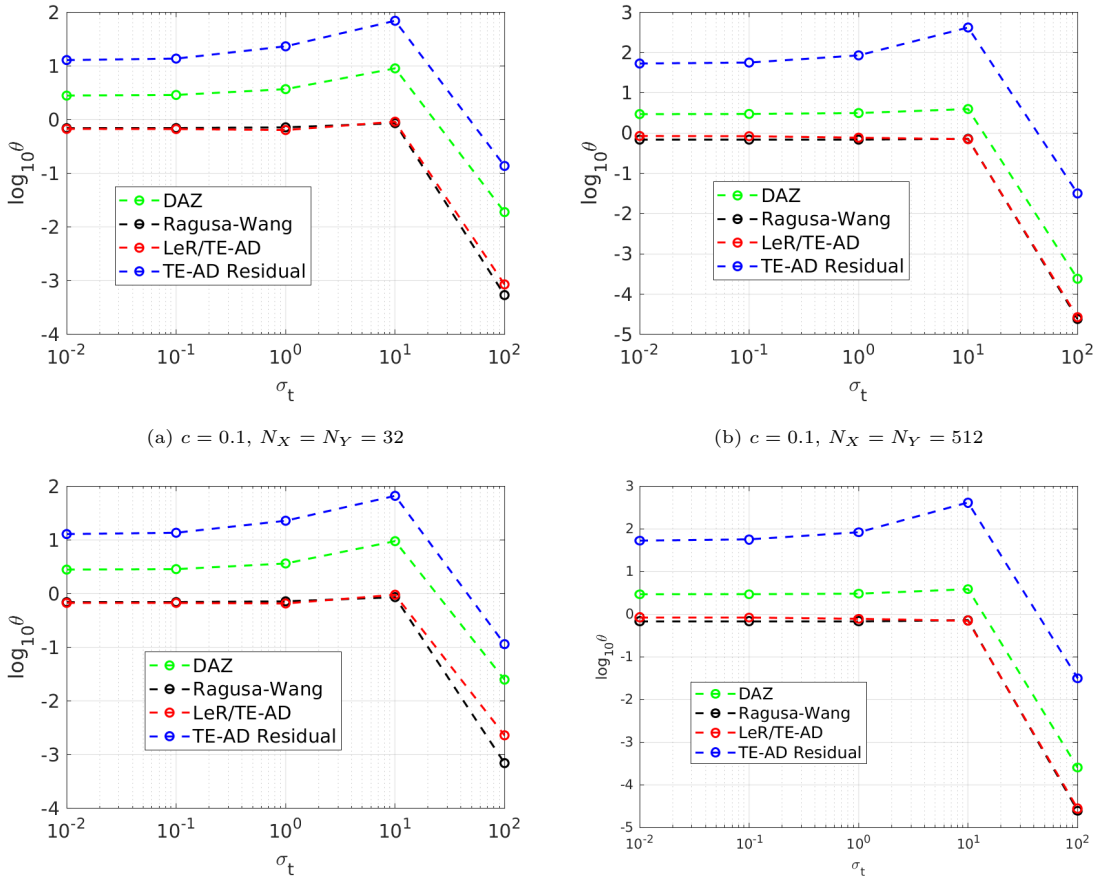

(a) $c = 0.1$, $N_X = N_Y = 32$

(b) $c = 0.1$, $N_X = N_Y = 512$

(c) $c = 0.9$, $N_X = N_Y = 32$

(d) $c = 0.9$, $N_X = N_Y = 512$

Figure 13: Global Effectivity Index vs. σ_t, Irregular Solution

The global effectivities of the estimators over the parameter range are plotted in Fig. 13 for irregular solutions and Fig. 14 for discontinuous solutions. For irregular solutions, LeR/TE-AD is the most accurate global error estimator, with RW being a very close second. For discontinuous solutions, RW is marginally superior to LeR/TE-AD on coarse meshes, but the trend is reversed for fine meshes. DAZ and the TE-AD residual both provide global bounds in all cases except the most optically thick $\sigma_t = 100.0$ cm^{-1} case. When the problem is very optically thick, the MMS solution is essentially flat aside from a thin boundary layer around the problem's periphery ([29, 22]), thus well approximated by a DGFEM-1 method. In effect, the assumption that other sources of error, *viz.* iterative error and computer roundoff error, are negligible is no longer true, and the resultant

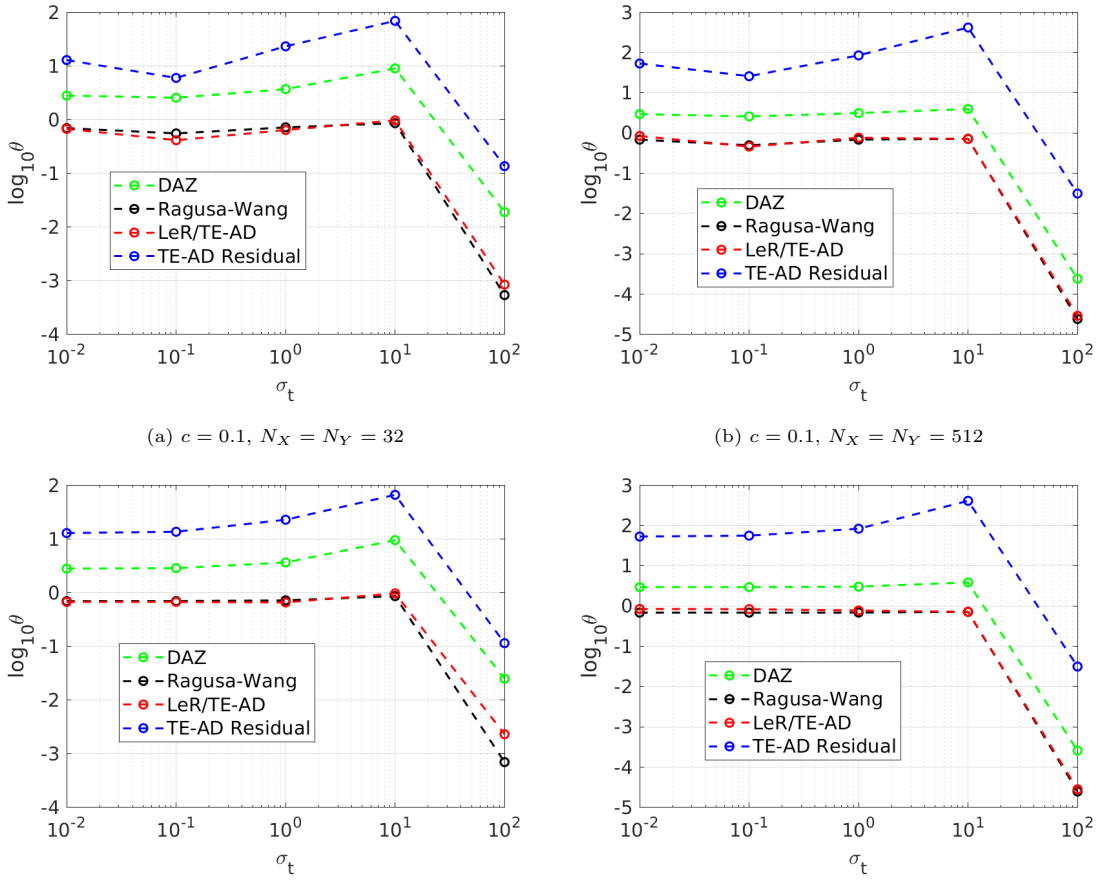

(a) $c = 0.1$, $N_X = N_Y = 32$

(b) $c = 0.1$, $N_X = N_Y = 512$

(c) $c = 0.9$, $N_X = N_Y = 32$

(d) $c = 0.9$, $N_X = N_Y = 512$

Figure 14: Global Effectivity Index vs. σ_t, Discontinuous Solution

spatial discretization error estimate is poor.

The local boundedness metric of the estimators over the parameter range are plotted in Fig. 15 for irregular solutions and Fig. 16 for discontinuous solutions. Aside from the special case of large optical thickness, the estimators that globally bound the error, DAZ and the TE-AD residual as an indicator, nearly universally locally bound the error for the problem set considered. Conversely, RW is predisposed to underestimate the local error, as it does the global error. However, LeR/TE-AD's local boundedness metric appears to be dependent on mesh refinement and optical thickness. The former can be explained by the fact that the truncated terms in Eqs. 19-22 may be large if not dominant at coarser meshes, indicating the solution is not yet asymptotically converging, leading to an underapproximated residual and, as a result, an underestimated error. The latter appears to be related to the SC-induced plume. In optically thin problems, the attenuation of the irregularities along the path of the SCs is weak, and the residual error within the plume is of greater magnitude.

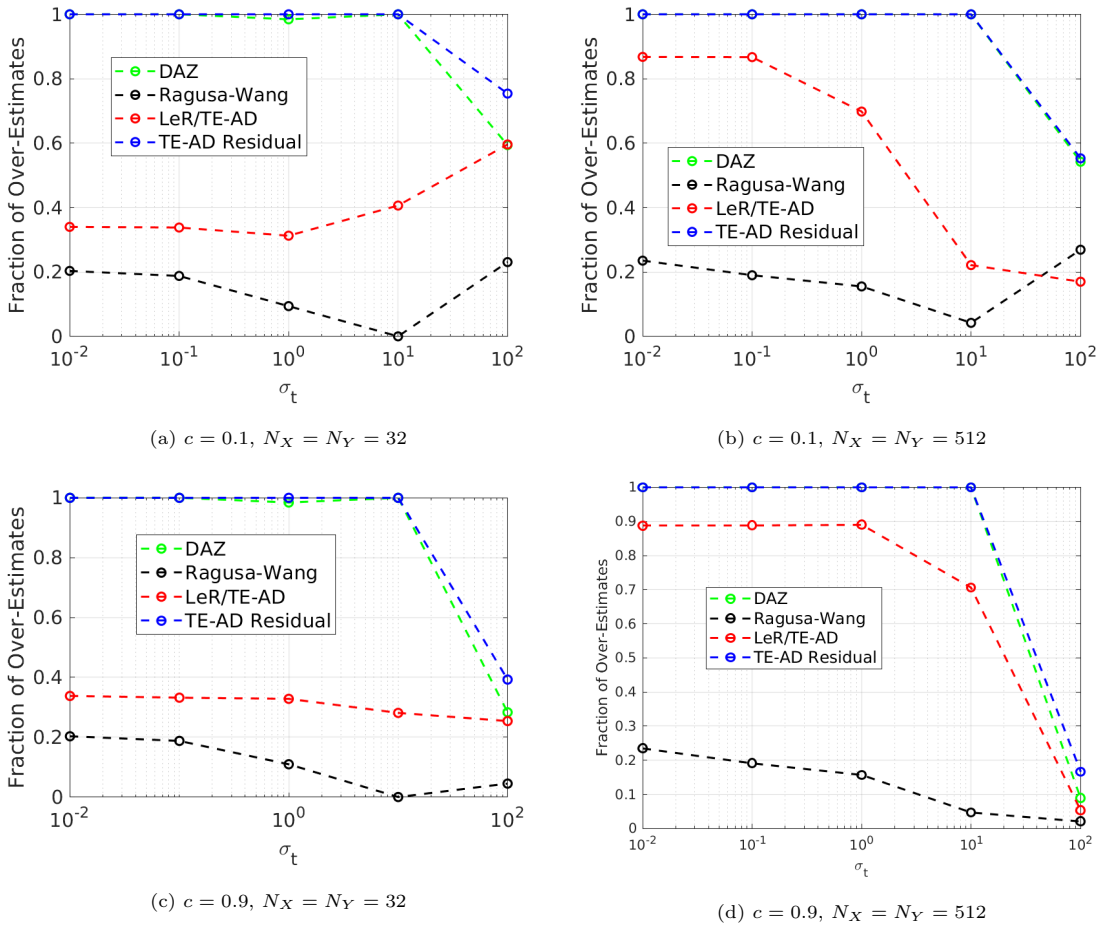

(a) $c = 0.1$, $N_X = N_Y = 32$

(b) $c = 0.1$, $N_X = N_Y = 512$

(c) $c = 0.9$, $N_X = N_Y = 32$

(d) $c = 0.9$, $N_X = N_Y = 512$

Figure 15: Local Boundedness vs. σ_t, Irregular Solution

This effect is re-enforced by the increase in the metric for the $\sigma_t = 10.0$ case for discontinuous solutions versus irregular solutions.

The accuracy metric of the estimators over the parameter range with values of $\beta = [10\%, 25\%, 50\%]$ are plotted in Fig. 17 for irregular solutions and Fig. 18 for discontinuous solutions. In instances where DAZ has no cells with estimates in the metric range, it is omitted. Neither DAZ nor the TE-AD residual as an indicator are appreciably accurate for this set of problem configurations, but as they are intended as global error bounds, this is unsurprising. In contrast to the DGFEM-0 results ([24]), RW is superior to LeR/TE-AD in most instances, with the exception of the most restrictive ($\beta = 10\%$) relative error bound for optically thick problems. As seen in the case study, LeR/TE-AD is double penalized by the error transport problem numerically spreading errors incurred by the residual approximation.

Furthermore, a second special case, $\sigma_t = 0.1$ and $c = 0.1$, is exposed. For discontinuous solutions

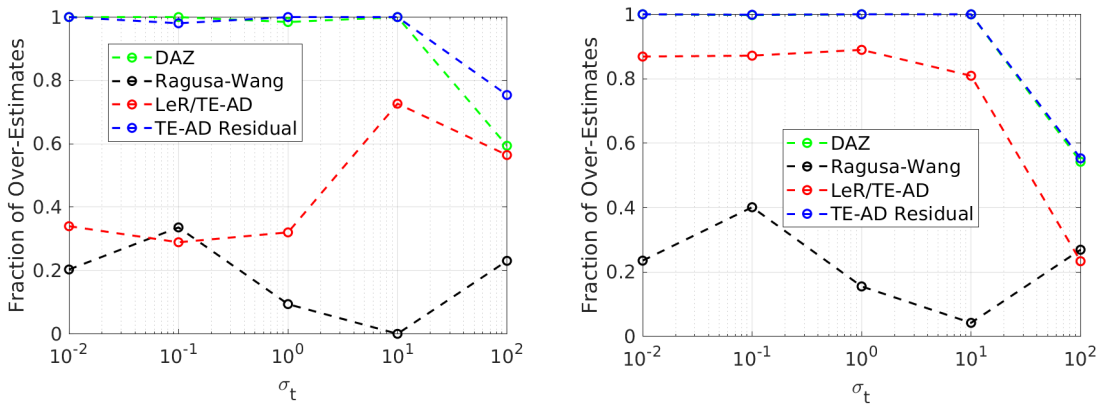

(a) $c = 0.1$, $N_X = N_Y = 32$

(b) $c = 0.1$, $N_X = N_Y = 512$

(c) $c = 0.9$, $N_X = N_Y = 32$

(d) $c = 0.9$, $N_X = N_Y = 512$

Figure 16: Local Boundedness vs. σ_t, Discontinous Solution

with low scattering ratio, as the optical thickness decreases, the solution's spatial profile becomes more linear on either side of the SC. At very low optical thickness, i.e., $\sigma_t = 0.01$, there is very little attenuation of the discontinuity by the host materials, thus there is a large source of spatial discretization error. However, at the optical thickness $\sigma_t = 0.1$, the increased attenuation of the discontinuities and linear behavior of the solution combine to produce near-zero errors at many points within the domain, thus breaking the assumptions of spatial discretization error estimation, *viz.*, that the iterative and floating point errors are negligible when compared to the spatial discretization error.

The precision metric of the estimators over the parameter range, plotted in Fig. 19 for irregular solutions and Fig. 20 for discontinuous solutions, demonstrate an overall decrease in precision for LeR/TE-AD, whereas RW and DAZ generally improve aside from the degenerate cases. Once again, this is due to the double penalization of LeR/TE-AD caused by the error transport problem and

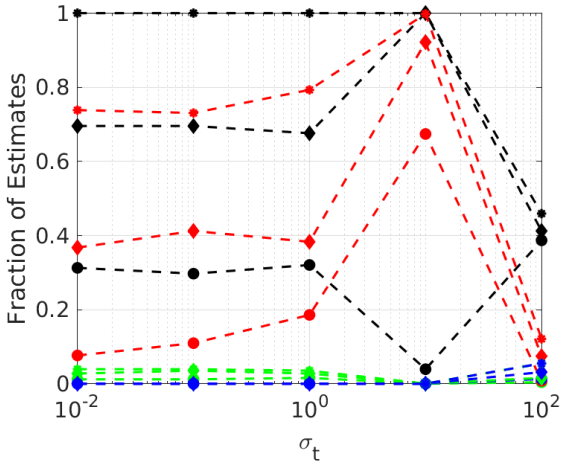

(a) $c = 0.1$, $N_X = N_Y = 32$

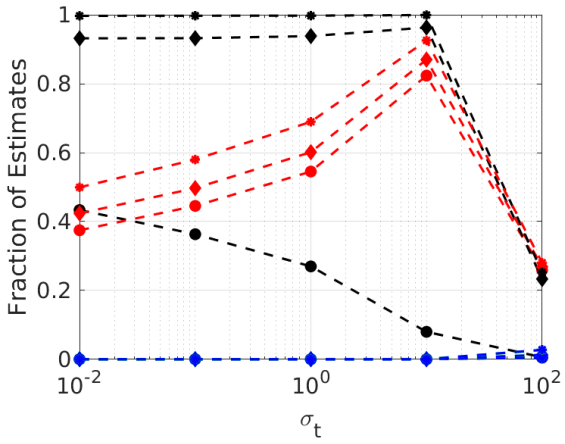

(b) $c = 0.1$, $N_X = N_Y = 512$

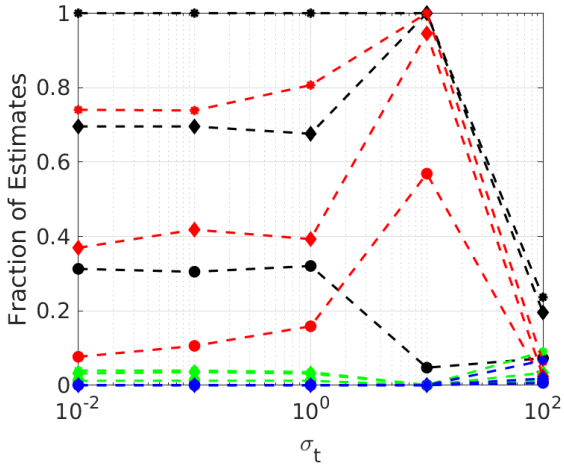

(c) $c = 0.9$, $N_X = N_Y = 32$

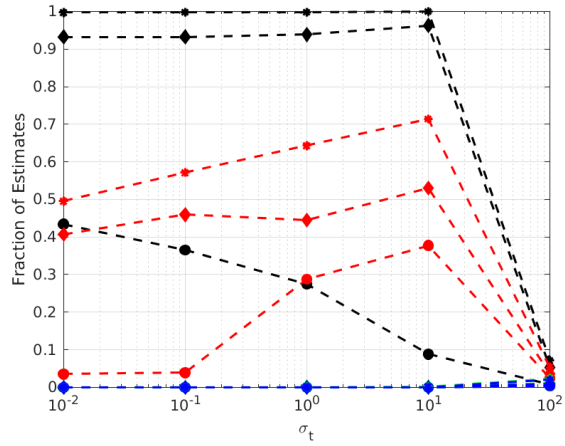

(d) $c = 0.9$, $N_X = N_Y = 512$

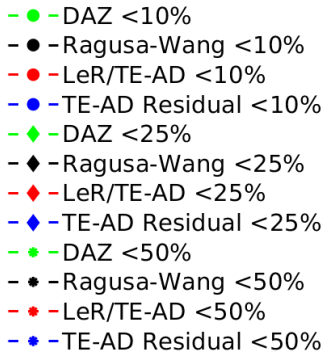

(e) Legend

Figure 17: Accuracy vs. σ_t, Irregular Solutions

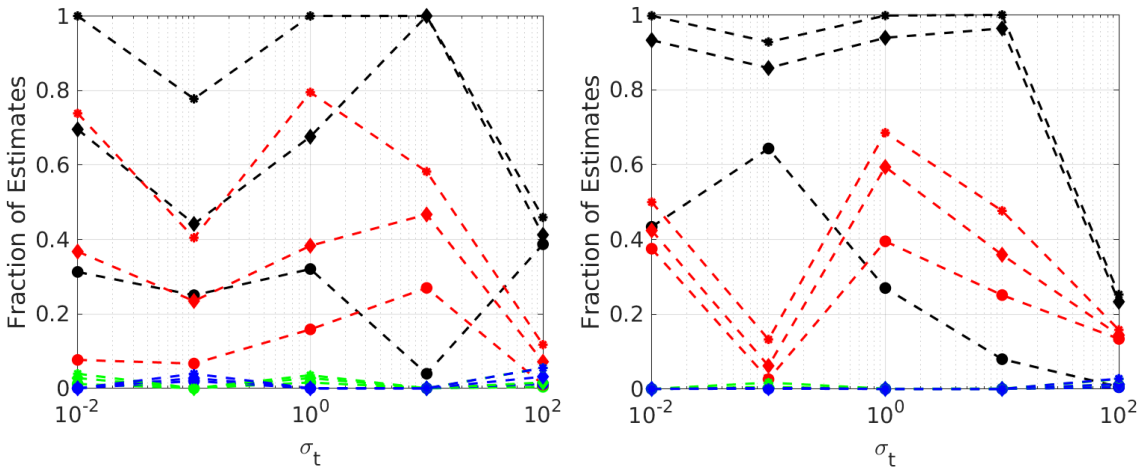

(a) $c = 0.1$, $N_X = N_Y = 32$

(b) $c = 0.1$, $N_X = N_Y = 512$

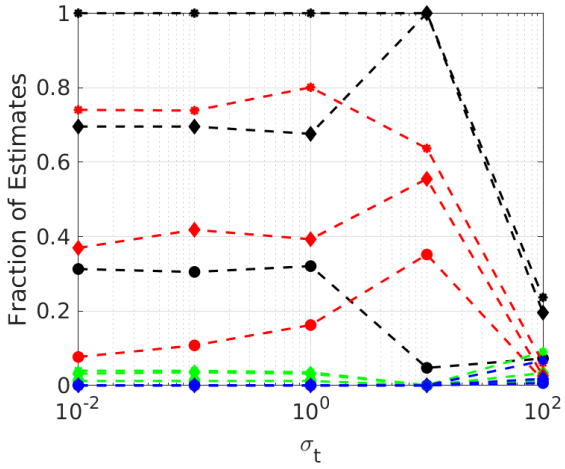

(c) $c = 0.9$, $N_X = N_Y = 32$

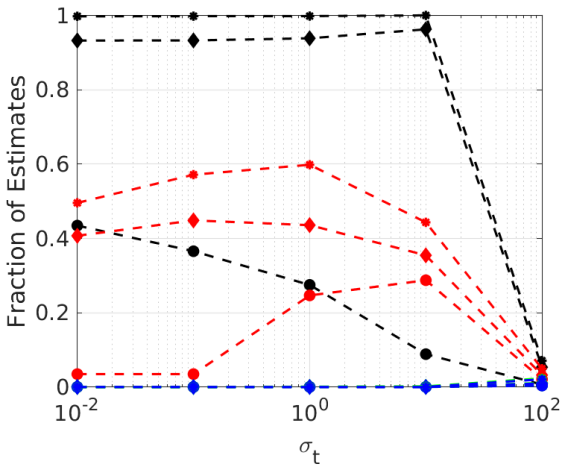

(d) $c = 0.9$, $N_X = N_Y = 512$

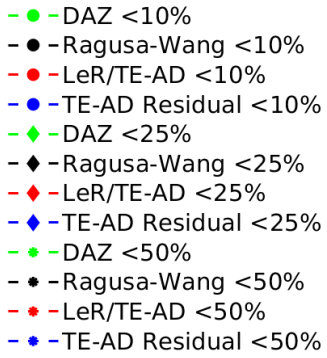

(e) Legend

Figure 18: Accuracy vs. σ_t, Discontinuous Solutions

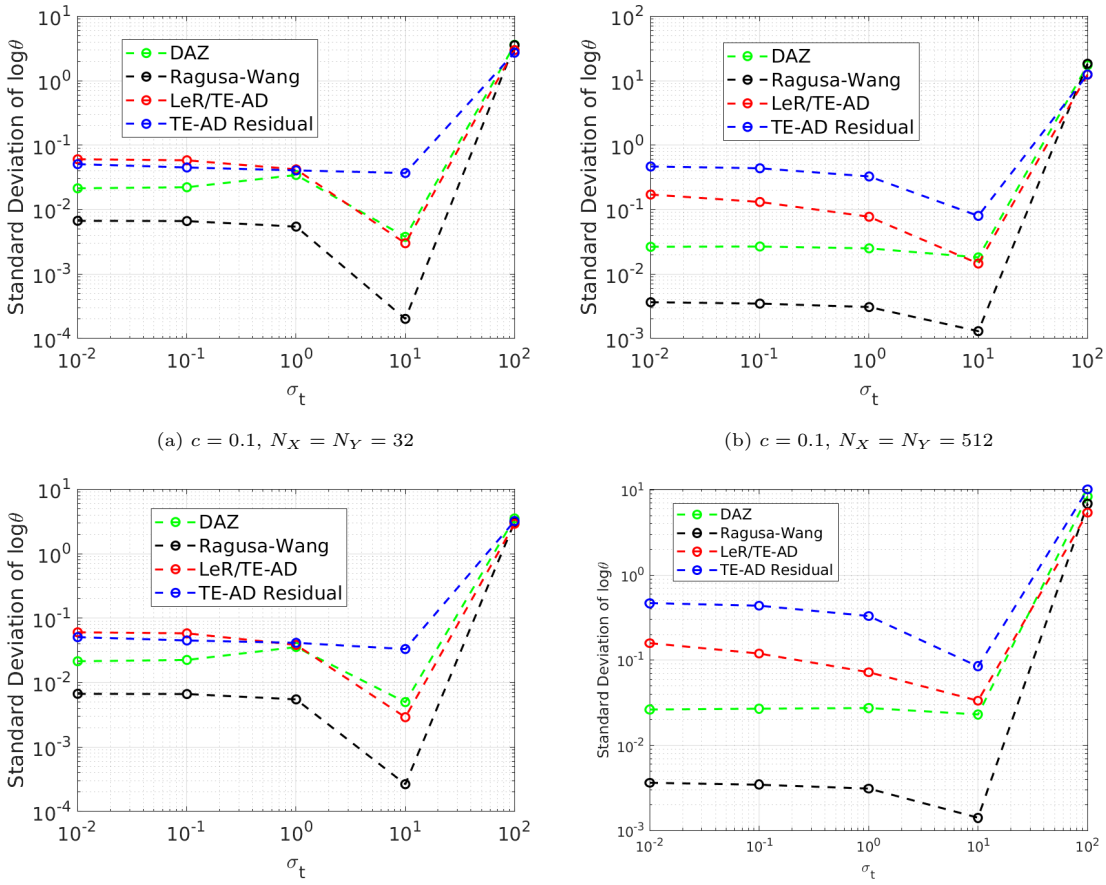

(a) $c = 0.1$, $N_X = N_Y = 32$

(b) $c = 0.1$, $N_X = N_Y = 512$

(c) $c = 0.9$, $N_X = N_Y = 32$

(d) $c = 0.9$, $N_X = N_Y = 512$

Figure 19: Precision vs. σ_t, Irregular Solutions

the large relative error in the residual approximation in the plume caused by irregularities limiting local accuracy of the numerical solution.

Finally, the computational cost of each estimator is plotted in Fig. 21 for irregular solutions and Fig. 22 for discontinuous solutions. RW is typically the most computationally expensive estimator, as it requires an additional auxiliary solution with four times as many unknowns, in this 2D configuration, as the original numerical solution. However, this cost is mitigated somewhat by the preconditioning. Thus, LeR/TE-AD, whose auxiliary solution requires the same number of unknowns as the numerical solution, is usually 1.5-3 times less computationally expensive than RW, and in some instances it actually takes longer to run than RW. However, the special case $c = 0.9$ and $\sigma_t = 0.1$ with discontinuous solution causes the computational cost of LeR/TE-AD to jump appreciably. This is caused by LeR/TE-AD failing to reach the iterative error convergence criterion, and instead hitting the maximum number of iterations. On closer inspection, the cell with maximum

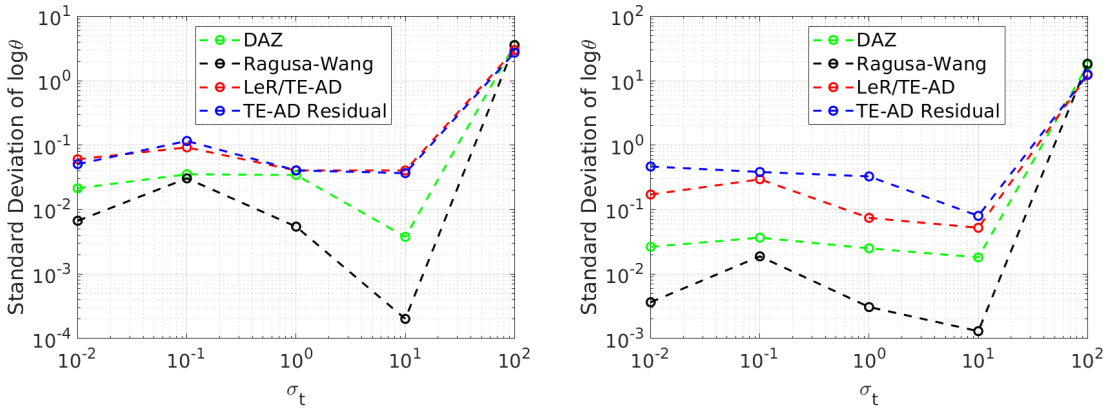

(a) $c = 0.1$, $N_X = N_Y = 32$

(b) $c = 0.1$, $N_X = N_Y = 512$

(c) $c = 0.9$, $N_X = N_Y = 32$

(d) $c = 0.9$, $N_X = N_Y = 512$

Figure 20: Precision vs. σ_t, Discontinuous Solutions

iterative error oscillates about the value 2.4×10^{-8}, and it has near-zero estimated and true error in the angular flux, so it would be considered sufficiently converged in an absolute sense, but fails the set stopping criterion. Thus, this case illustrates the potential pitfall of an iterative auxiliary solution[5]. DAZ is more computationally expensive than LeR/TE-AD for cases that require few iterations by the latter to reach the iterative stopping criterion, but as this number increases, DAZ maintains its computational cost supremacy, since it does not require an iterative auxiliary solution.

[5]Preliminary testing has shown that reasonably reducing the iterative error stopping criterion for the auxiliary transport problems has little negative effect on the error estimate so long as the iterative error is small *vis-a-vis* the spatial discretization error, and can serve to both reduce computational cost of the estimators and prevent "runaway" iterations.

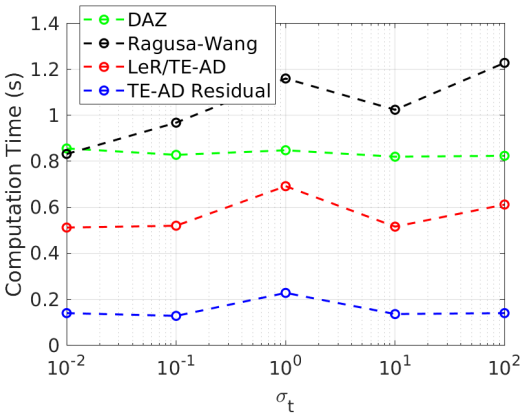

(a) $c = 0.1$, $N_X = N_Y = 32$

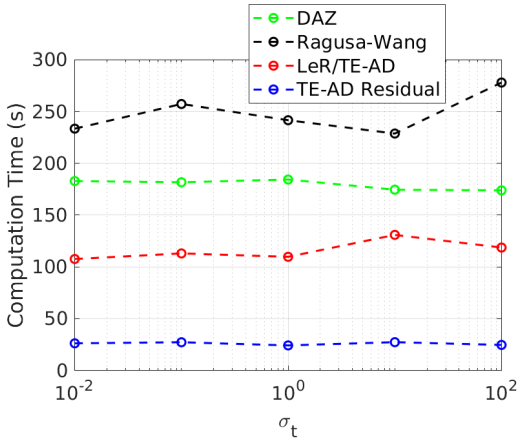

(b) $c = 0.1$, $N_X = N_Y = 512$

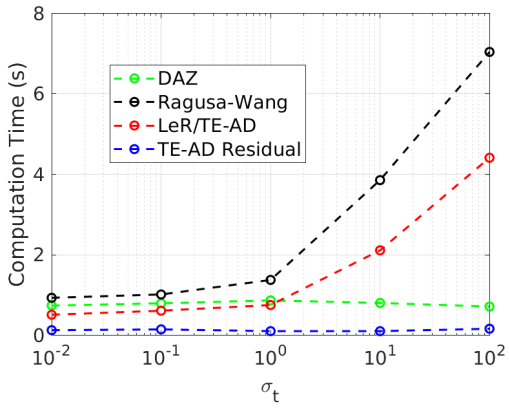

(c) $c = 0.9$, $N_X = N_Y = 32$

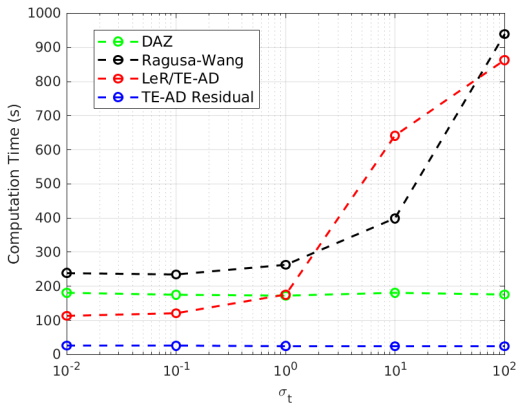

(d) $c = 0.9$, $N_X = N_Y = 512$

Figure 21: Computational Cost vs. σ_t, Irregular Solutions

3.3. MMS Evaluation Conclusions

While LeR/TE-AD is still useful for estimating global and local solution accuracy and tends to overestimate the error locally, it significantly suffers in increasing method order from $\Lambda = 0$ to $\Lambda = 1$ from the capped local accuracy of the numerical solution due to solution regularity characteristic of practical configurations. RW, in contrast, improves in accuracy and precision, and DAZ improves in precision. LeR/TE-AD is uniquely affected by this phenomenon because local errors in the residual approximation are spread globally by the auxiliary error transport problem, whereas other estimators deposit their errors merely locally.

However, RW and DAZ are both refinement-based estimators. RW directly approximates the numerical solution with h-refinement, and DAZ uses a pseudo Λ-refinement to generate the residual and jump terms that build the local contributions to the error bound. Thus, for this MMS set of

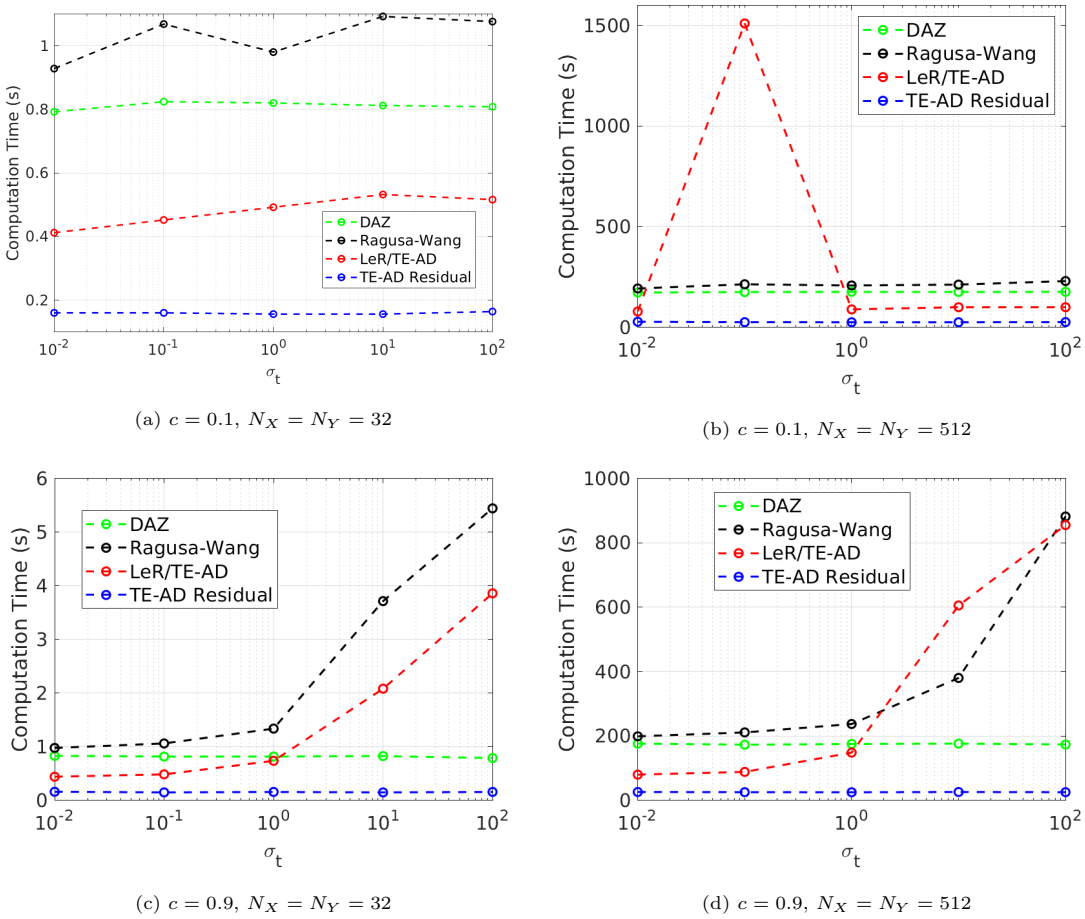

(a) $c = 0.1$, $N_X = N_Y = 32$

(b) $c = 0.1$, $N_X = N_Y = 512$

(c) $c = 0.9$, $N_X = N_Y = 32$

(d) $c = 0.9$, $N_X = N_Y = 512$

Figure 22: Computational Cost vs. σ_t, Discontinuous Solutions

problems, in which many derivative terms are nil, a refinement of a DGFEM-1 solution will be of particularly high quality, and it is likely that these two estimators are at least somewhat biased to exhibit superior performance than they would attain in a more realistic configuration. This conjecture is borne by the numerical tests reported in Sec. 4.

4. Realistic Problem Geometry Evaluation

To examine a less ideal sequence of problems and avoid potential biasing of estimators' performance due to nil solution moments as mentioned in Sec. 3.3, the estimators are evaluated for non-MMS realistic problem geometries. A Richardson Extrapolation procedure ([38]) is utilized to generate reference solutions, and the refinement sequence is chosen to ensure that it does not intersect the space of the numerical solutions in order to prevent potential biasing. That is, if for each case we obtain DGFEM-0 and DGFEM-1 solutions on a $N_x \times N_y$ mesh, the refinement sequence is performed on DGFEM-2 solutions with $N'_x \times N'_y = [4N_x \times 4N_y, 8N_x \times 8N_y, 16N_x \times 16N_y]$. The choice of $\Lambda = 2$ and omission of $N'_x \times N'_y = 2N_x \times 2N_y$ in the sequence are intended to further prevent biasing of the refinement-based estimators.

Because multigroup spatial discretization error estimation is a nascent field of investigation ([39]) and to conform with our previous evaluations, the realistic problems are uncoupled in energy and examined as one-speed problems. Three benchmark configurations are employed: the C5G7 benchmark unreflected UO_2 assembly fast and thermal groups, and a dogleg duct shielding problem. In each case, the true solution is irregular in the first derivative across SCs.

4.1. Fast C5G7 UO_2 Assembly

The 2D C5G7 benchmark is a reactor mini-geometry established for the verification of neutron transport codes ([40, 41]). The original benchmark is a multigroup problem, with seven energy groups, and it has seven material compositions. The modified version utilized in this work isolates a single UO_2 assembly, depicted as part of a quarter-geometry in Fig. 23, as a fixed source problem with explicit BCs. Each square in Fig. 23 corresponds to a pin cell geometry detailed in Fig. 24, where the diameter of the fuel-clad mix is 1.08 cm, and the length of each side of the square pin cell is 1.26 cm (note that we only consider the 2D benchmark, so height details are omitted, but additional geometry details can be found in [41]). The material that makes up the "fuel-clad mix" regime in Fig. 24 is denoted by the legend at the bottom of Fig. 23. Each assembly contains 17×17 pin cells, giving single assembly dimensions of 21.42 cm × 21.42 cm. A 14×14 square mesh is overlaid on each pin cell, with no further homogenization, corresponding to Fig. 25, where red cells are metal (fuel or other material) and white cells are moderator (note that the total area of the red cells does not conserve the area of the undiscretized fuel pin). This corresponds to a 238×238 mesh over the entire single assembly used in our reduced model. Note that the material composition per cell remains invariant over mesh refinement levels.

For the fast group, the material properties of $g = 1$ from [41] are used, also shown in Table 1, and scattering ratios are computed with the in-group scattering cross-sections. To keep consistent

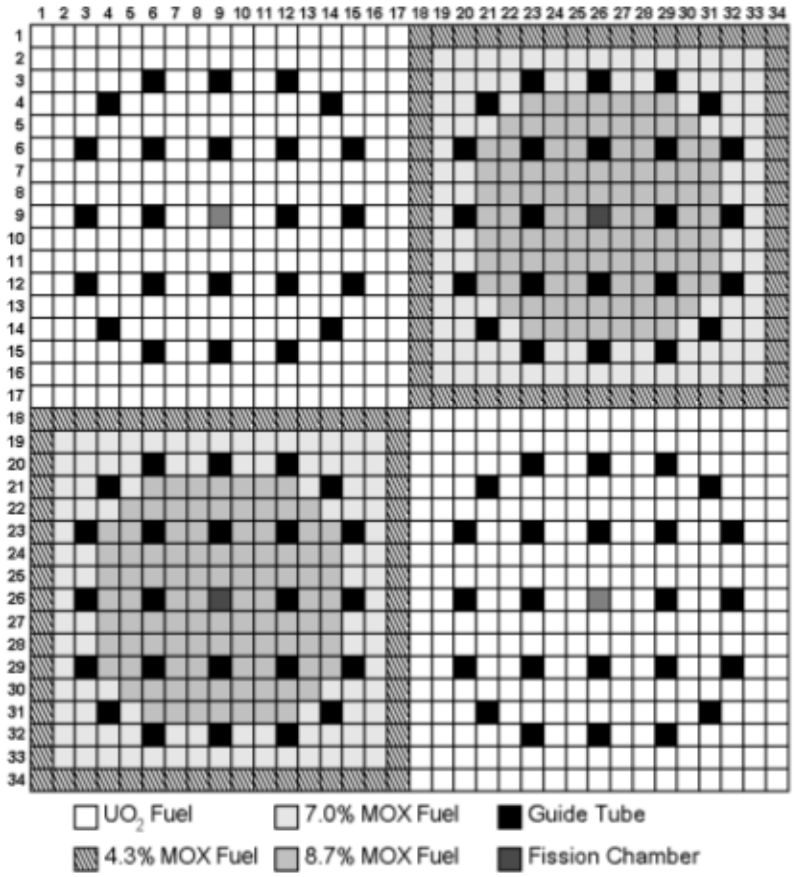

Figure 23: C5G7 Assembly Geometry (Without the Reflector Layer) [41]

Material	σ_t (cm^{-1})	c
UO_2 Fuel	2.12450E-01	0.600315
Fission Chamber	1.90730E-01	0.346909
Guide Tube	1.90730E-01	0.346909
Moderator	2.30070E-01	0.193322

Table 1: Fast Group Material Properties ([41])

with previous work, which only utilized non-multiplying materials, the materials are treated as non-fissioning. However, to mimic the neutron source in the fast group, the fixed source in fuel cells is set to unity. BCs are set to zero. Because the total cross section of the materials is in the optically thin region, per the parameters of the MMS evaluation, we would expect the irregularities across SCs to remain largely non-smooth, and therefore produce worse error estimates.

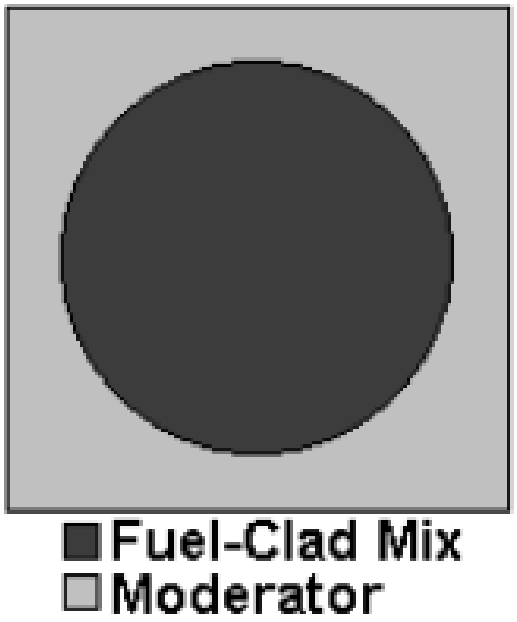

Figure 24: C5G7 Fuel Pin Geometry [41]

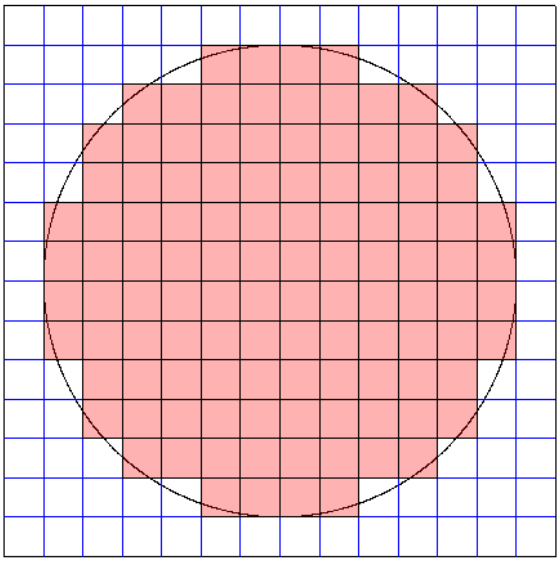

Figure 25: Square Mesh Discretization of Fuel Pin for 238×238 Mesh

The diamond fractal-like pattern of the reference scalar flux solution[6] for S_4 LS quadrature[7]

[6]The Richardson Extrapolation that led to the DGFEM-0 reference solution had 7.0% of scalar flux moments non-monotonic and 24.5% of angular flux moments non-monotonic. This difference is expected, since the scalar flux is an integrated quantity; thus, non-dominant and non-monotonic behavior is more likely to be suppressed in the

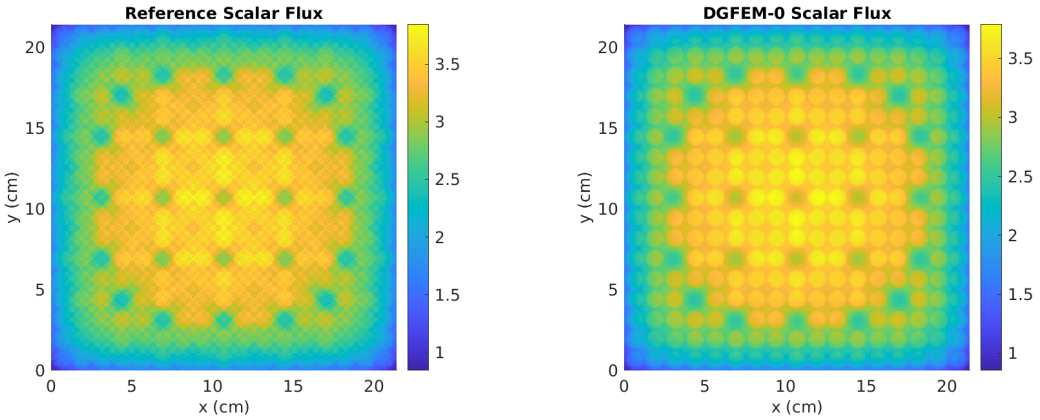

(a) Reference

(b) DGFEM-0

Figure 26: Cell-Average Scalar Flux Solution, Fast Group

on a 238×238 mesh, depicted in Fig. 26(a), demonstrates the preponderance of SCs in a realistic problem, and the corresponding DGFEM-0 solution, Fig. 26(b), cannot capture the spatial behavior of the reference solution.

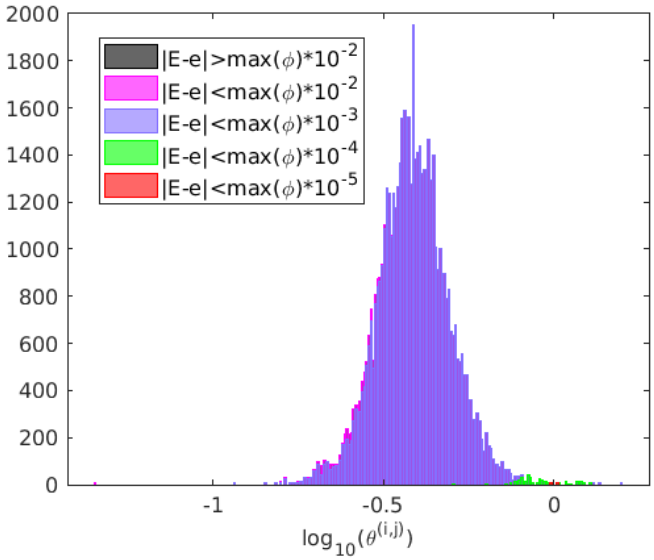

Figure 27: Fast Group: LeR/TE-AD $\log_{10}$ Local Effectivity Index Histogram, DGFEM-0

The three selected estimator histograms for DGFEM-0, Figs. 27-29, demonstrate that for non-

summed quantity.

[7]Note that while this pattern indicates a poor angular discretization, this is irrelevant when evaluating the spatial discretization error, per the definition in Eq. 7.

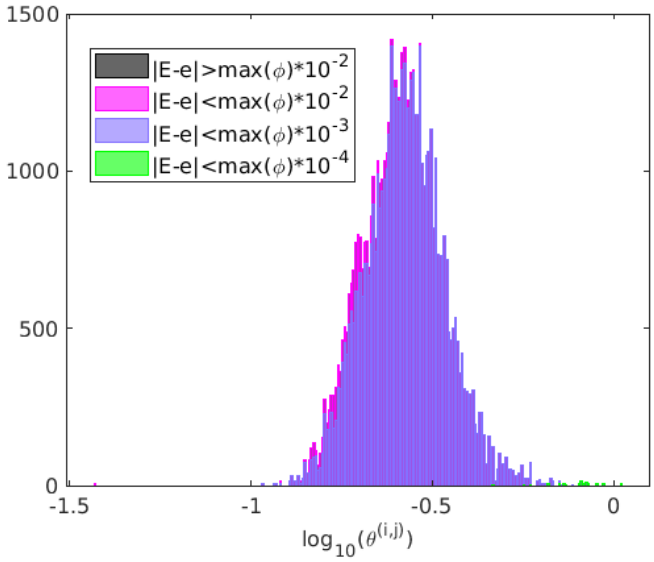

Figure 28: Fast Group: RW $\log_{10}$ Local Effectivity Index Histogram, DGFEM-0

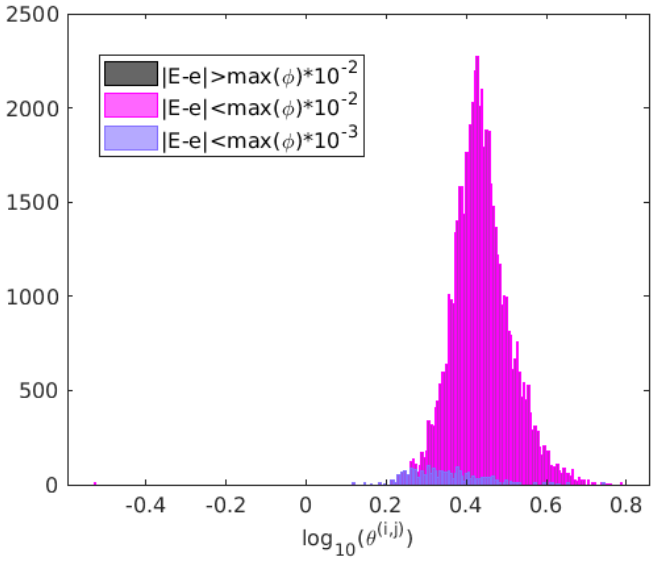

Figure 29: Fast Group: DAZ $\log_{10}$ Local Effectivity Index Histogram, DGFEM-0

MMS problems, the estimators exhibit far worse precision and accuracy than before. All three estimators exhibit roughly the same overall range of effectivities and comparable peak widths. DAZ is marginally more accurate than LeR/TE-AD in terms of peak distance from $\log_{10} \theta^{(i,j)} = 0$, which is, in turn, marginally more accurate than RW. In an absolute sense, the error in the error estimate is generally in the fourth decimal point of the maximum scalar flux's magnitude.

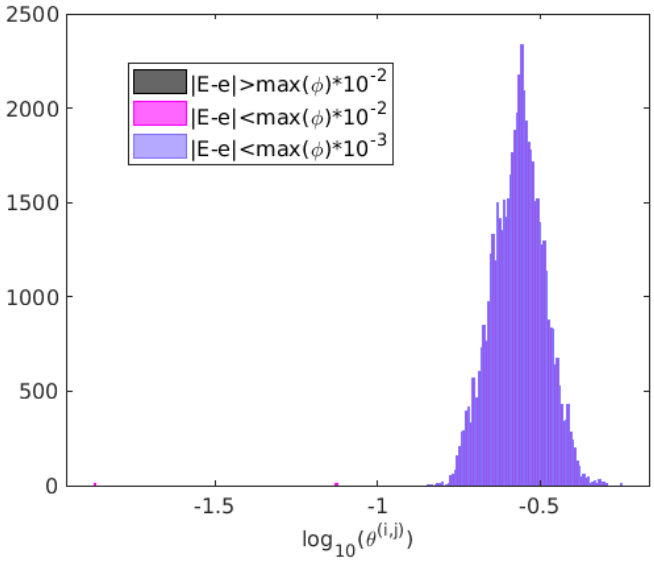

Figure 30: Fast Group: LeR/TE-AD $\log_{10}$ Local Effectivity Index Histogram, DGFEM-1

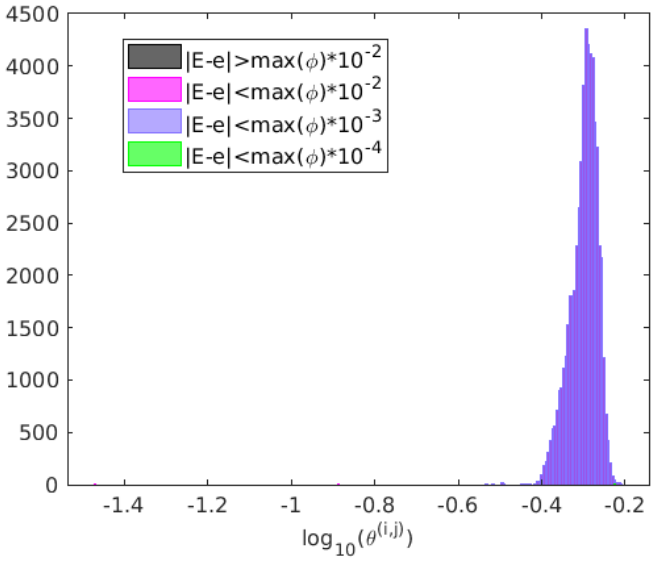

Figure 31: Fast Group: RW $\log_{10}$ Local Effectivity Index Histogram, DGFEM-1

In increasing the numerical method's order from $\Lambda = 0$ to $\Lambda = 1$[8], LeR/TE-AD suffers a reduction in relative and absolute accuracy, Fig. 30. The former was anticipated from the MMS study in

[8]Associated Richardson Extrapolation for DGFEM-1 reference solution had 9.2% of scalar flux moments non-monotonic and 22.0% of angular flux moments non-monotonic.

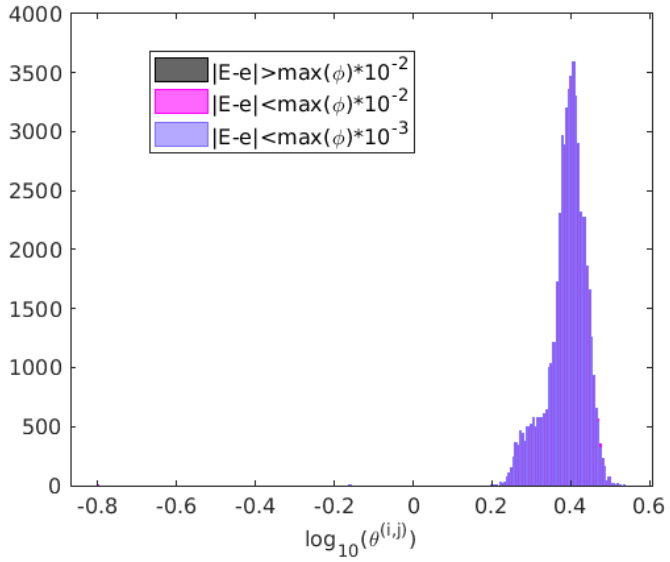

Figure 32: Fast Group: DAZ $\log_{10}$ Local Effectivity Index Histogram, DGFEM-1

Sec. 3, in which LeR/TE-AD saw worse accuracy metrics across the parameter range for a DGFEM-1 discretization versus DGFEM-0 ([24]). The latter is reflective of the complex geometry; the true and estimated errors are not as small as they are in the MMS problems. RW, on the other hand, Fig. 31, exhibits better accuracy and precision for DGFEM-1, but the effectivity distribution is noticeably worse than that for the MMS case study, Fig. 10, with reduced peak height, precision, and accuracy. DAZ, Fig. 32, improves in precision for $\Lambda = 1$.

	DGFEM-0		DGFEM-1	
Estimator	$\log_{10}\theta$	Time (s)	$\log_{10}\theta$	Time (s)
Numerical Solution	–	5.34	–	17.1
LeR/TE-AD	-0.417	8.74	-0.560	29.1
RW	-0.583	20.4	-0.301	66.2
DAZ	0.424	7.84	0.380	36.6

Table 2: Global Effectivity, Fast Group

The global effectivities of the estimators more or less align with the peak location of the local effectivity index, Table 2. DAZ maintains its advantage as a bound on global error from above in non-degenerative problems. LeR/TE-AD consumes almost two times the execution time of the numerical solution, suggestive of a configuration and residual approximation that produce an error

transport problem requiring more iterations. RW is slightly less than four times the cost of the numerical solution, which is reflective of the $h/2$-mesh solution computational cost, plus pre- and post-processing, minus the reduction in cost from preconditioning the refined solution.

4.2. Thermal C5G7 UO_2 Assembly

The total cross sections and scattering ratios for the thermal group associated with each material in the UO_2 assembly described in the previous section are given in Table 3. Compared to the fast

Material	σ_t (cm^{-1})	c
UO_2 Fuel	5.70610E-01	0.478576
Fission Chamber	1.43450E+00	0.766190
Guide Tube	1.43450E+00	0.766204
Moderator	3.30570E+00	0.750431

Table 3: Thermal Group Cross-Sections ([41])

group data, Table 1, here the total cross sections and scattering ratios are larger. Because of the former, the irregularities across the SCs will be attenuated to a greater degree, thereby smoothing the true solution. Furthermore, the moderator cells have fixed source set to unity, and the BCs are set to unity, in order to mimic downscatter of fission neutrons into the thermal group within the assembly and their reflection or in-leakage from teh assembly's surroundings.

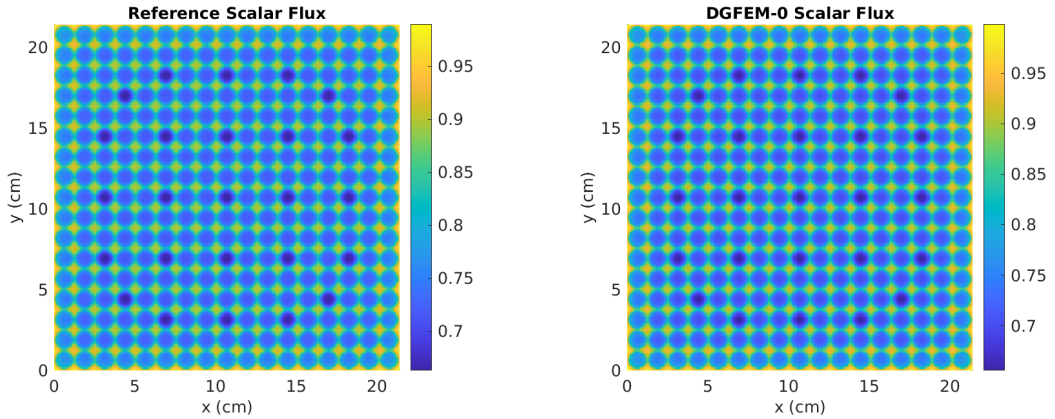

(a) Reference

(b) DGFEM-0

Figure 33: Cell-Average Scalar Flux Solution, Thermal Group

The reference solution[9], Fig. 33(a), indeed is smoother than its fast-group counterpart. As a result, the DGFEM-0 numerical solution, Fig. 33(b), visually matches the reference.

From the LeR/TE-AD histogram for DGFEM-0, Fig. 34, we observe that the estimate is more precise, both in terms of peak width and overall range of effectivities, than the fast group problem,

[9] 4.4% of scalar flux moments and 14.8% of angular flux moments are non-monotic in the Richardson Extrapolation.

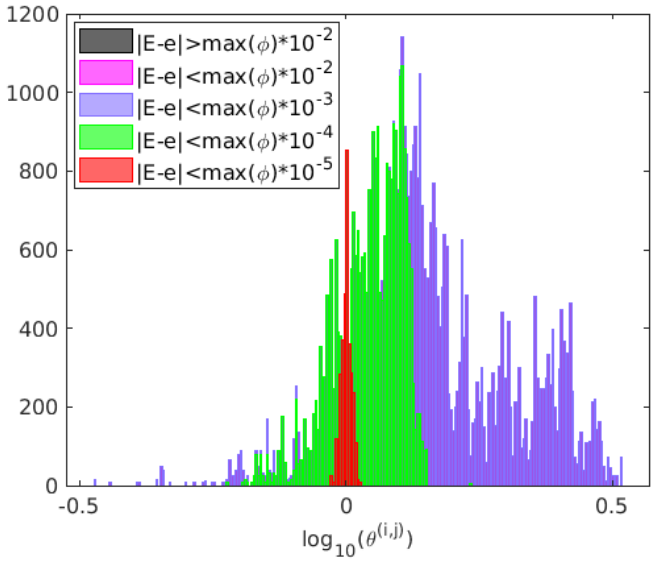

Figure 34: Thermal Group: LeR/TE-AD $\log_{10}$ Local Effectivity Index Histogram, DGFEM-0

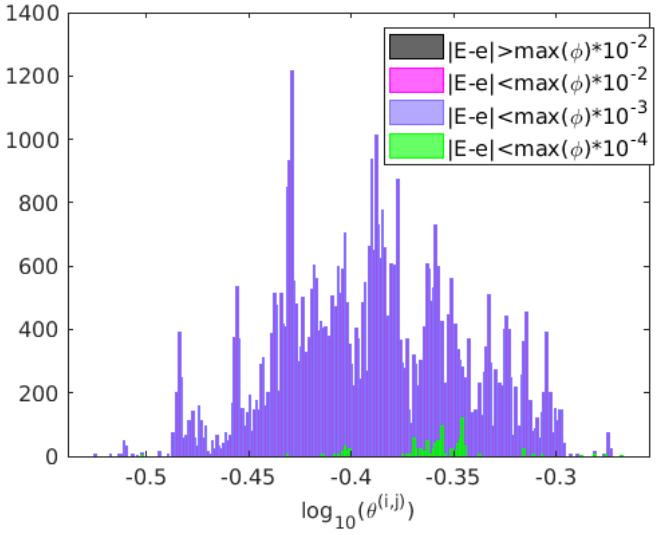

Figure 35: Thermal Group: RW $\log_{10}$ Local Effectivity Index Histogram, DGFEM-0

and the estimate is accurate in both a relative and absolute sense. RW, Fig. 35, incurs a large increase in precision, with all values being contained in a narrow range, but the location of the mean value underestimates the reference error by over a factor of 2. DAZ appears to be less precise for this problem due to the presence of many subpeaks, Fig. 36, and it also overestimates the error to a greater degree than the fast group, thus reducing its accuracy.

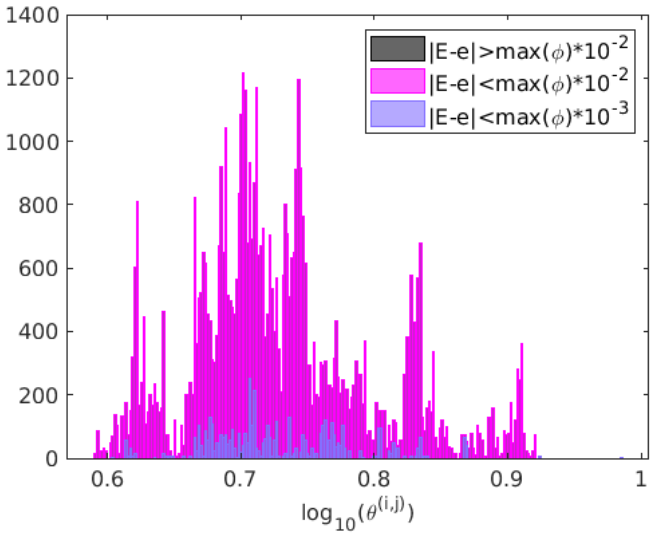

Figure 36: Thermal Group: DAZ $\log_{10}$ Local Effectivity Index Histogram, DGFEM-0

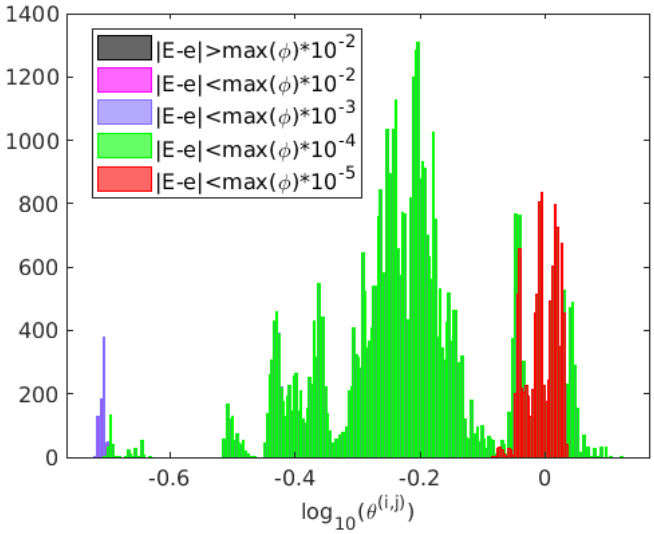

Figure 37: Thermal Group: LeR/TE-AD $\log_{10}$ Local Effectivity Index Histogram, DGFEM-1

The LeR/TE-AD estimate, Fig. 37, for the DGFEM-1 solution[10] demonstrates less precision, due to the prominent subpeak separated from the main peak. However, the two peaks are accurate, particularly the smaller subpeak. The other noticeable difference between this and the DGFEM-0

[10] 12.7% of scalar flux moments and 11.4% of angular flux moments are non-monotonic in the Richardson Extrapolation.

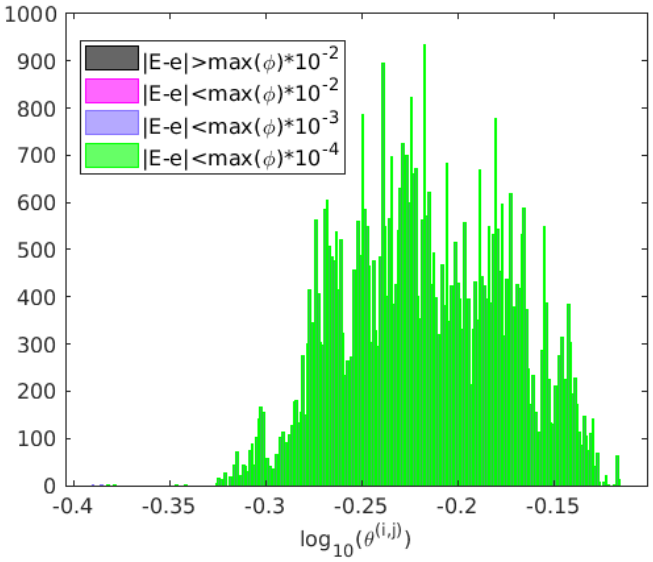

Figure 38: Thermal Group: RW $\log_{10}$ Local Effectivity Index Histogram, DGFEM-1

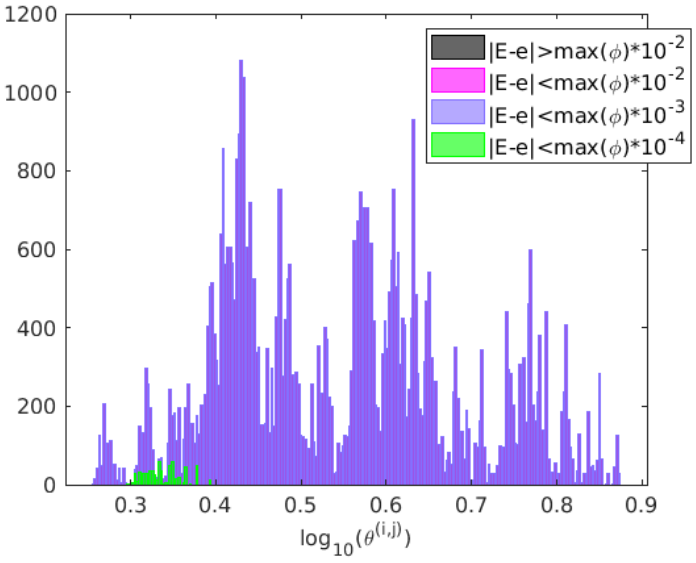

Figure 39: Thermal Group: DAZ $\log_{10}$ Local Effectivity Index Histogram, DGFEM-1

estimate is that the DGFEM-1 estimate largely underestimates the error. RW is more precise in its range of values for DGFEM-1, and the mean value is closer to agreement with the true error. DAZ is even less precise, but still provides total local boundedness from above. Again, the global effectivities of the estimators reflect the peak location of the local effectivity index, Table 4. Because of the greater scattering ratios, the iterative methods take longer to converge versus the fast group;

	DGFEM-0		DGFEM-1	
Estimator	$\log_{10}\theta$	Time (s)	$\log_{10}\theta$	Time (s)
Numerical Solution	–	10.7	–	39.0
LeR/TE-AD	0.169	14.5	-0.140	63.6
RW	-0.399	31.3	-0.210	105
DAZ	0.746	7.45	0.628	37.6

Table 4: Global Effectivity, Thermal Group

however, the computation time of DAZ is essentially unchanged from the fast group problem.

We desire to use the angular flux error estimator strategies to directly estimate the error in a dependent quantity of interest. Because LeR/TE-AD and RW directly compute ϵ_h^Λ, the error in any quantity derived from the angular flux can be directly estimated by these estimators. However, because DAZ is computed as local norm contributions to a global bound, a heuristic must be applied. We consider a hypothetical scenario where a reactor physicist wishes to know the contribution of the spatial discretization error to the total error in the pin-wise fission rate densities for the purpose of error analysis. He or she therefore seeks an estimate of the error in the average thermal fission rate density in each pin cell (for these purposes, the fission chamber will be treated as non-multiplying). The pin cell-wise average error in the fission rate density is calculated by,

$$E_{pin}^{(v,w)} = \frac{\int_{\mathcal{B}^{(v,w)}} dA\ \sigma_f(x,y)\xi_h^\Lambda(x,y)}{\int_{\mathcal{B}^{(v,w)}} dA}, \tag{35}$$

where σ_f is the macroscopic fission cross section[11], $\xi_h^\Lambda = \phi_h^\Lambda - \Pi_h^\Lambda\phi$ is the true error in the scalar flux, and $\mathcal{B}^{(v,w)}$ is the subdomain that contains all cells $K^{(i,j)}$ associated with a given pin cell containing UO_2 material, where $v, w = 1, \ldots, 17$. The global average error in the fission rate density is simply,

$$E_{pin} = \frac{1}{264}\sum_{v=1}^{17}\sum_{w=1}^{17} E_{pin}^{(v,w)}, \tag{36}$$

where the 264 factor is the number of pin cells that contain fuel. The estimated error in the average fission rate density is analogously

$$e_{pin}^{(v,w)} = \frac{\int_{\mathcal{B}^{(v,w)}} dA\ \sigma_f(x,y)\zeta_h^\Lambda(x,y)}{\int_{\mathcal{B}^{(v,w)}} dA}, \tag{37}$$

where $\zeta_h^\Lambda(x,y) = \sum_m^M w_m\epsilon_m(x,y)$, and Eq. 37 is only valid for LeR/TE-AD and RW. The true

[11] σ_f = 2.16004E-01 for UO_2 in the thermal group.

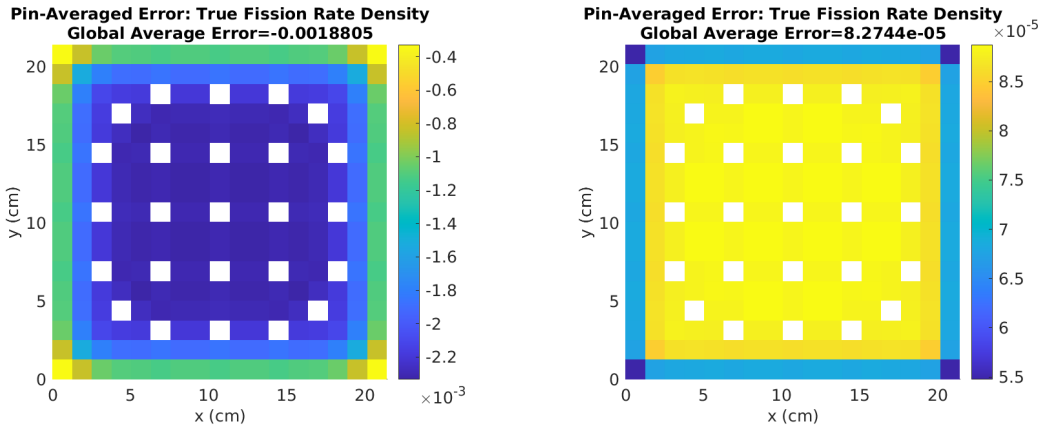

(a) DGFEM-0 (b) DGFEM-1

Figure 40: Thermal Group: True Error in Average Fission Rate Density

error[12] in the average fission rate density is plotted in Fig. 40. Given Fig. 33(a) and the fission cross section, the maximum solution error is in the second decimal place for the DGFEM-0 discretization and the fourth decimal place for DGFEM-1.

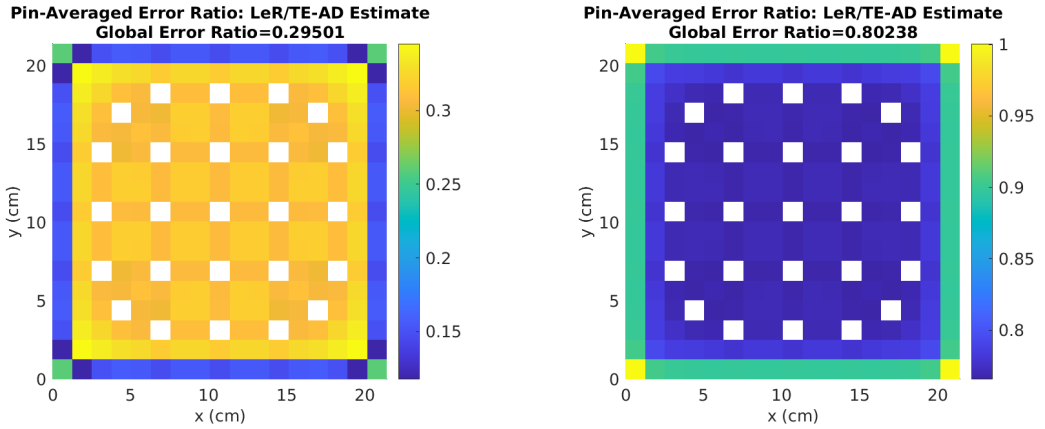

(a) DGFEM-0 (b) DGFEM-1

Figure 41: Thermal Group: LeR/TE-AD $\log_{10}|e_{pin}^{(v,w)}/E_{pin}^{(v,w)}|$

The $\log_{10}$-scale ratios of the resultant estimates for the error in the average fission rate density computed by LeR/TE-AD are shown in Fig. 41, and while the DGFEM-0 estimate overestimates the error in most pin cells by approximately a factor of two, the DGFEM-1 estimate grossly overestimates the error at almost an order of magnitude.

[12]All average fission rate densities were computed via Richardson Extrapolation, and all extrapolations are found to be monotonic.

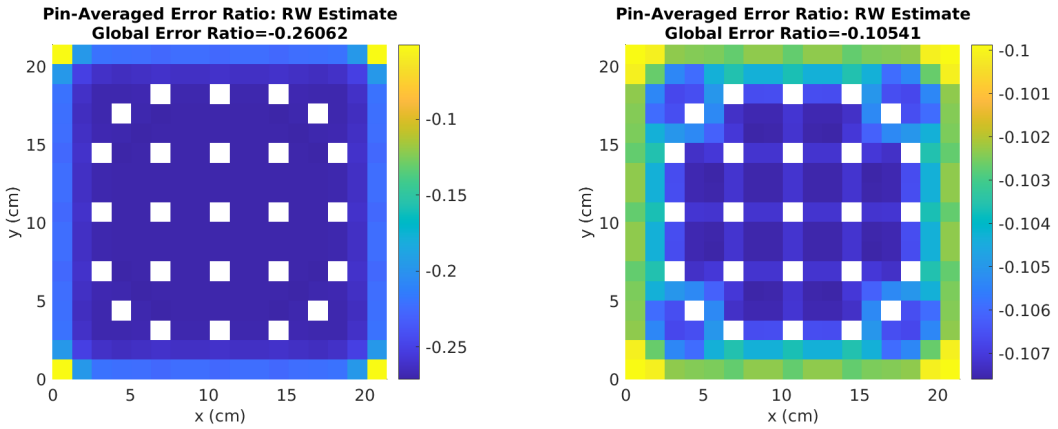

(a) DGFEM-0 (b) DGFEM-1

Figure 42: Thermal Group: LeR/TE-AD $\log_{10}|e_{pin}^{(v,w)}/E_{pin}^{(v,w)}|$

The RW estimate ratios, Fig. 42, are more accurate than LeR/TE-AD, and become more accurate with increasing Λ. However, unlike LeR/TE-AD, they do not locally bound the estimates of the average fission rate density.

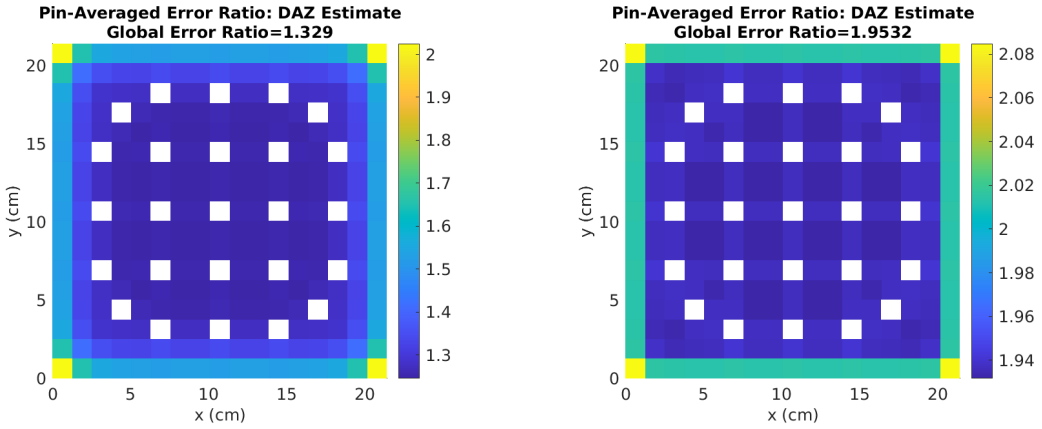

(a) DGFEM-0 (b) DGFEM-1

Figure 43: Thermal Group: LeR/TE-AD $\log_{10}|e_{pin,DAZ}^{(v,w)}/E_{pin}^{(v,w)}|$

Finally, the DAZ estimate ratios are plotted in Fig. 43. The heuristic applied to estimate the error in the average fission rate density is

$$e_{pin,DAZ}^{(v,w)} = \frac{1}{112} \sum_{(i,j),\forall K^{(i,j)} \in \mathcal{B}^{(v,w)}} \sigma_f^{(i,j)} \frac{e_{DAZ}^{(i,j)}}{\sqrt{\Delta x_i \Delta y_j}}, \tag{38}$$

where $\sigma_f^{(i,j)}$ is the fission cross section in cell $K^{(i,j)}$, the 112 factor is the number of cells per pin cell that have fuel in them, see Fig. 25, and taking the square root of the $K^{(i,j)}$ cell area keeps units

consistent on both sides of Eq. 38. One issue with Eq. 38 is that it only estimates the magnitude of the error, not its sign, due to its norm formulation that is necessarily non-negative. The resultant error estimate, though it provides a global bound, grossly overestimates the error by orders of magnitude. This is most likely due to the lack of cancellation of error in the cell-wise integration.

4.3. Dogleg Duct

The last test geometry considered is a dogleg duct shielding geometry based on [42]. The original

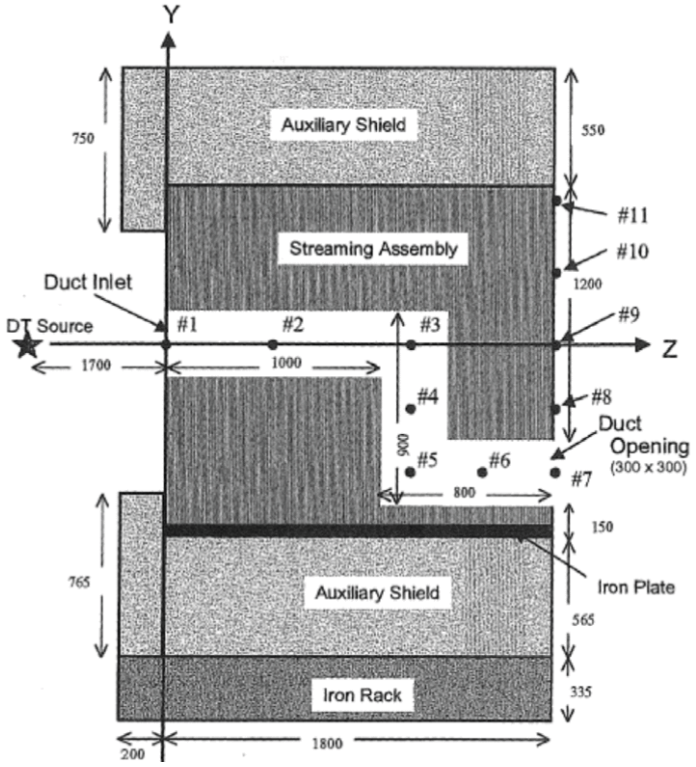

Figure 44: Dogleg Geometry from [42]

streaming assembly geometry, with measurements in mm, is given in Fig. 44. A 2D simplification of the geometry is modeled in Fig. 45, where the DT source of unit strength is repositioned to the duct inlet to alleviate primary ray effects, and a single detector is placed at location #7. As before, further restrictions to conform to previous studies are imposed: vacuum BCs on all external edges, one-group, steady-state, and isotropic scattering in all involved materials, and S_4 LS angular quadrature. A uniform 82×124 mesh is overlaid on the domain with cell size of 2.5 cm$\times$2.5 cm[13]. The material cross section data given in Table 5 is approximately based on actual neutron cross sections at 14 MeV for air, water (auxiliary shield), iron, and stainless steel (streaming assembly), taken from the ENDF database ([43]). Here too, while these modifications distinguish the employed configuration from the original benchmark, our goal is to make the configuration amenable to generating an accurate reference solution against which only the spatial discretization error is judged. The reference

[13]In the simplified geometry, the Auxilliary Shield height is increased by 10 mm and the Iron Rack height is decreased by 10 mm to utilize the uniform mesh.

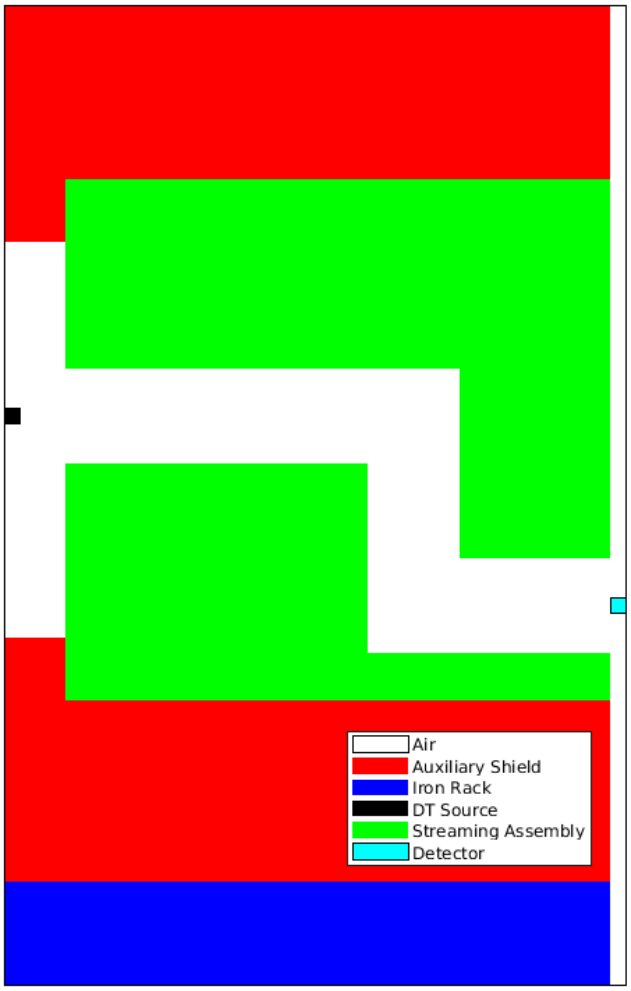

Figure 45: Simplified Dogleg Geometry

Material	σ_t (cm^{-1})	c
Air	1.2E-04	0.833
Auxiliary Shield	3.0E-01	0.767
Iron Rack	2.9E-01	0.828
DT Source	1.2E-04	0.833
Streaming Assembly	3.5E-01	0.943
Detector	1.2E-04	0.833

Table 5: Dogleg Materials Nuclear Data, Approximately Computed from [43]

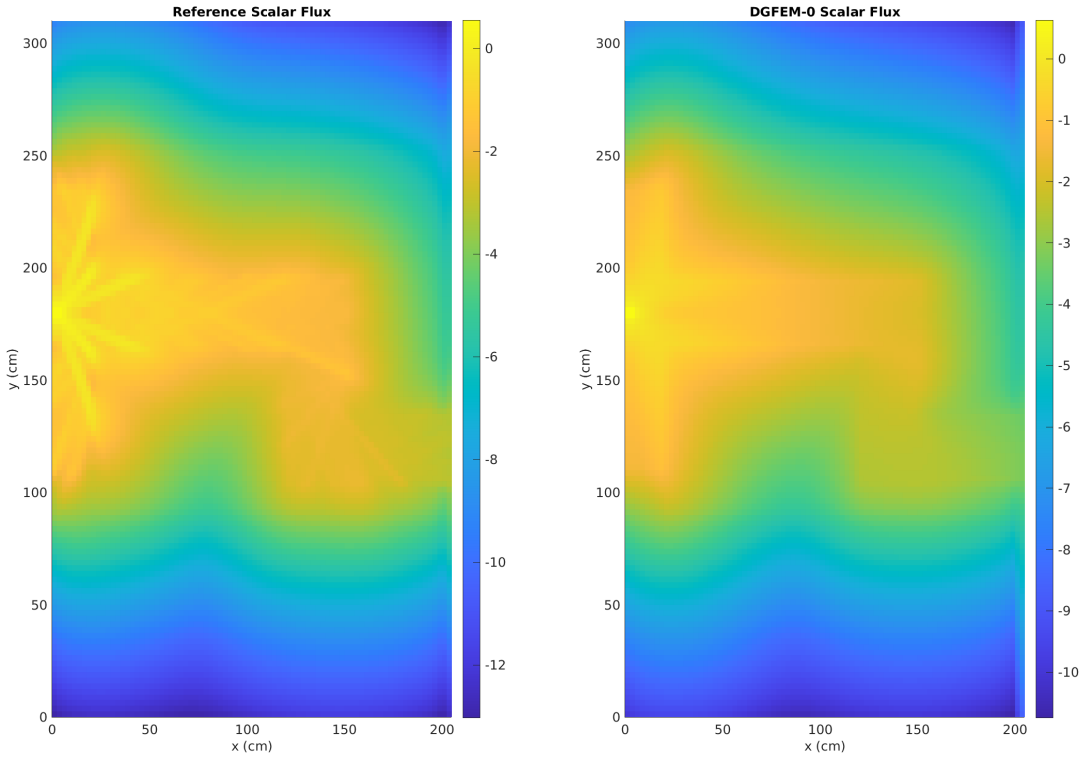

(a) Reference

(b) DGFEM-0

Figure 46: Cell-Average Scalar Flux Solution $\log_{10}$-Scale, Dogleg

solution[14] is plotted against the DGFEM-0 scalar flux solution in Fig. 46, both on $\log_{10}$-scale.

[14] 17.3% of scalar flux moments and 18.1% of angular flux moments are non-monotonic in the DGFEM-0 Richardson Extrapolation.

The reference solution displays strong ray effects along SCs near the DT source, which are much suppressed in the DGFEM-0 solution due to numerical diffusion of particles near SC trajectories emanating from the point-like source. In both cases, the solution is noticeably of greater magnitude at the duct outlet than in the shielded region.

	DGFEM-0		DGFEM-1	
Estimator	$\log_{10}\theta$	Time (s)	$\log_{10}\theta$	Time (s)
Numerical Solution	–	11.3	–	44.1
LeR/TE-AD	-0.392	11.9	-0.306	43.0
RW	-0.606	41.3	-0.162	137
DAZ	4.88	1.85	1.51	6.70

Table 6: Global Effectivity, Dogleg Duct

The global effectivities and computation times are listed in Table 6. For this case, which requires more iterations than either C5G7 problem, the estimators requiring iterative solutions are more computationally expensive. DAZ has a computational time that is proportional to the number of unknowns in the problem. In terms of effectivity index, however, DAZ grossly overestimates the error for both Λ, consistent with a previously-identified reduction in the quality of the HOPS in problems that require more iterations ([23]). LeR/TE-AD is superior to RW for the DGFEM-0 discretization, but they flip for the DGFEM-1 discretization[15], although LeR/TE-AD's global error estimate is slightly improved. However, because the true solution has a linear shape in the shield owing to the high absorption, the refinement-based estimators may disproportionately benefit from a DGFEM-1 discretization for this problem.

Rather than examine the local effectivity index for this problem, we acknowledge that the hypothetical engineer modelling a shield is not interested in the error distribution within the shield or the duct, but only at the detector/duct outlet. Therefore, the estimated error in the DGFEM-0 scalar flux as a function of the y-coordinate at $x = 205$ cm is plotted in Fig. 47. In the true error, Fig. 47(a), the duct outlet is manifested as a sharp decline in the error's profile. The peaks and troughs are associated with reflected ray effects along SCs. LeR/TE-AD overestimates the magnitude of the error by approximately a factor of 3, but accurately portrays the location of the error dip. However, it does not capture the finer details of the error peaks and troughs, unlike RW, which

[15] 23.1% of scalar flux moments and 23.0% of angular flux moments are non-monotonic in the DGFEM-1 Richardson Extrapolation.

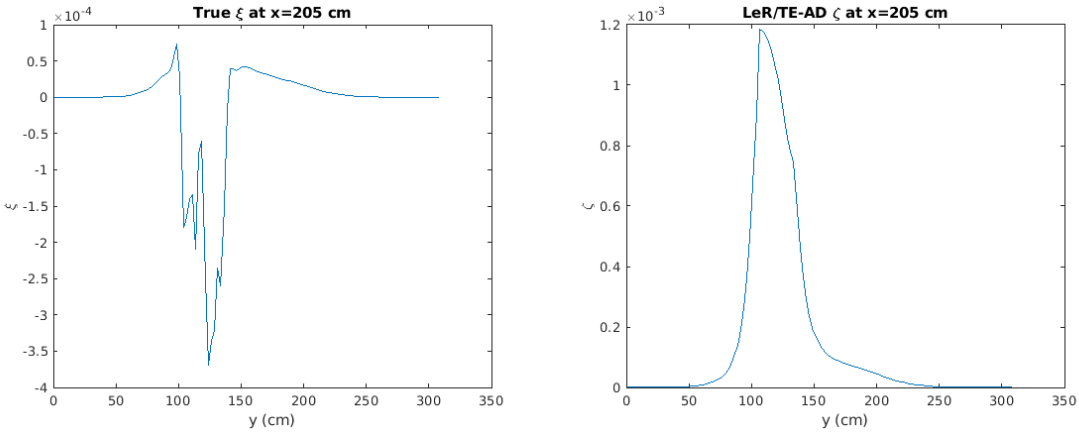

(a) True Error

(b) LeR/TE-AD Estimate

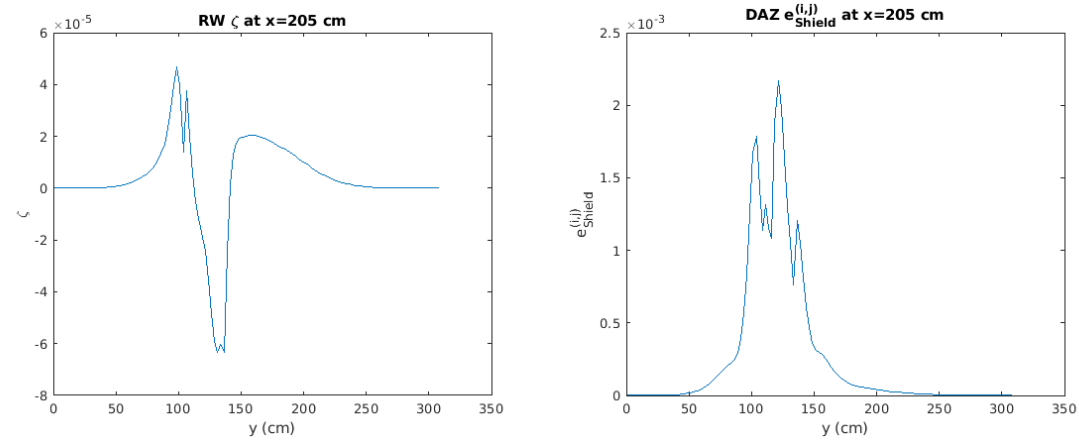

(c) RW Estimate

(d) DAZ Estimate

Figure 47: Error in Shielded Scalar Flux, DGFEM-0

underestimates the true error in a relative sense. In the case of DAZ, the plotted heuristic is

$$e^{(i,j)}_{Shield} = \frac{e^{(i,j)}_{DAZ}}{\sqrt{\Delta x_i \Delta y_j}}, \tag{39}$$

which is by nature non-negative. DAZ arguably best captures the peaks and troughs of the error, but cannot capture the sign of the error, and overestimates the error by almost an order of magnitude.

The same quantities are plotted for the DGFEM-1 discretization in Fig. 48, and demonstrate that the true error for a linear discretization is far more oscillatory near the SCs due to the non-monotonicity of higher-order methods. LeR/TE-AD again cannot capture the oscillation of the true error in the duct outlet due to the imprecision in the residual approximation in cells near the SCs, and it overestimates the magnitude of the error by about a factor of 2. RW captures the spatial behavior of the true error very well, but also underestimates the magnitude of the error. DAZ is

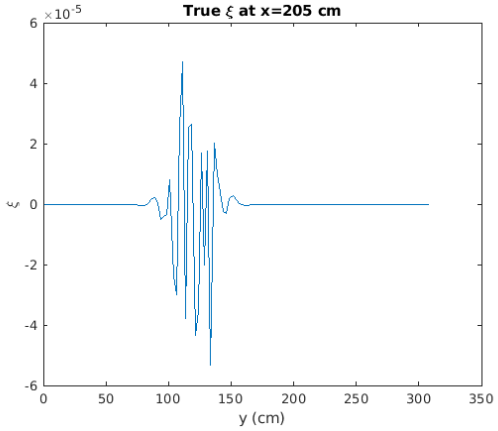

(a) True Error

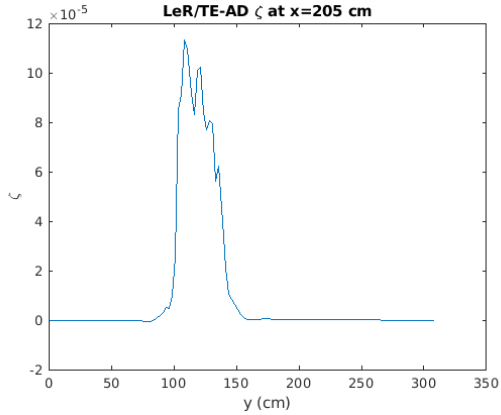

(b) LeR/TE-AD Estimate

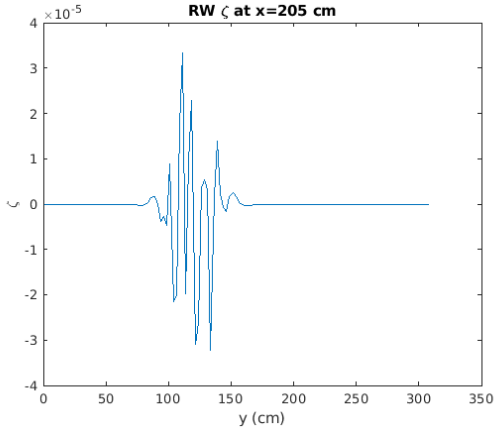

(c) RW Estimate

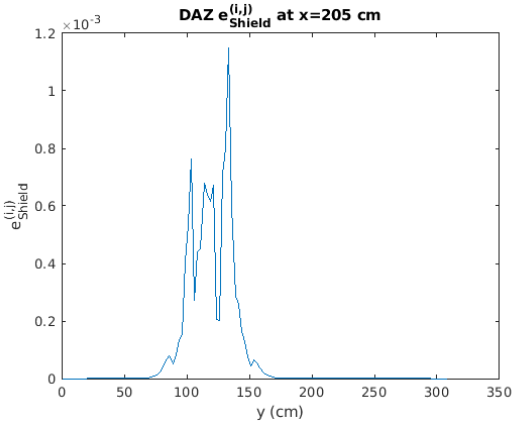

(d) DAZ Estimate

Figure 48: Error in Shielded Scalar Flux, DGFEM-1

less able to capture the shape of the error for the DGFEM-1 discretization, and it overestimates the error by over an order of magnitude.

The detector-averaged scalar flux (as a surrogate for response) error estimate is also computed[16]. The true error in the detector is

$$E_D = \frac{\int_{\mathcal{F}} dA\ \xi_h^{\Lambda}(x,y)}{\int_{\mathcal{F}} dA}, \tag{40}$$

where $\mathcal{F}$ is the subdomain that contains all cells $K^{(i,j)}$ associated with the detector, and the estimated error in the detector for RW or LeR/TE-AD is,

$$e_D = \frac{\int_{\mathcal{F}} dA\ \zeta_h^{\Lambda}(x,y)}{\int_{\mathcal{F}} dA}. \tag{41}$$

[16]The detector-averaged scalar flux is monotonic in both Richardson Extrapolations.

An analogous heuristic is applied to DAZ to generate the detector-averaged error estimate

$$e_{D,DAZ} = \frac{1}{4} \sum_{(i,j),\forall K^{(i,j)} \in \mathcal{F}} \frac{e_{DAZ}^{(i,j)}}{\sqrt{\Delta x_i \Delta y_j}}. \tag{42}$$

The resultant error relative to the DT source's unit strength is shown in Table 7. For both method

	DGFEM-0		DGFEM-1	
	Error	$\log_{10}\lvert e_D/E_D\rvert$	Error	$\log_{10}\lvert e_D/E_D\rvert$
True	-3.268E-04	0.000E+00	-1.709e-05	0.000E+00
LeR/TE-AD	1.914E-03	7.676E-01	1.860E-04	1.037E+00
RW	-4.334E-05	-8.774E-01	-1.007E-05	-2.295E-01
DAZ	2.640E-03	9.073E-01	8.084-04	1.675E+00

Table 7: Detector Error in Average Flux, Dogleg, DGFEM-0

orders, LeR/TE-AD and DAZ overestimate the error to a great degree. However, LeR/TE-AD is the most accurate estimate for DGFEM-0, due to the gross underestimation by RW. For DGFEM-1, though, RW is the most accurate by far, and in both cases it is the only estimator to achieve the correct sign of the true error.

5. Conclusions

Previously, we have developed a novel "residual source estimator", an implicit residual-based spatial discretization error estimator, for S_N particle transport methods and assessed its performance for a DGFEM-0 scheme, finding it to provide a precise and accurate error estimate at a lower computational burden than a refinement-based scheme. In this work, the necessary residual and derivative approximations were derived, and the estimator's performance was assessed for a DGFEM-1 scheme on a case study and with a parameter-wide metric-based approach using MMS-generated test problems.

On the MMS suite, LeR/TE-AD typically generates an estimate of the error within an order of magnitude of the true error in most spacial cells, but despite favorable results, it does not fare as well as it did for DGFEM-0. Conversely, the more accurate numerical method here leads to a greatly enhanced error estimate for two contemporary estimators, RW and DAZ; however, the resultant distribution of effectivity indices for LeR/TE-AD is less precise, and often more inaccurate, despite the higher order numerical solution. It was ultimately determined that local inaccuracies in the numerical solution near true solution irregularities incur greater relative error in the derivative approximations (and, by extension, the residual approximation), which is numerically spread

through the domain in the error transport problem. Additionally, all considered estimators were evaluated on a set of realistic problem configurations, with reference solutions obtained via Richardson extrapolation, for DGFEM-0 and DGFEM-1 schemes. The results highlight the consequence of using MMS, specifically homogeneous medium, as the large number of singular characteristics in heterogeneous configurations cause all the considered error estimators to be less accurate or precise than the MMS study would imply. Furthermore, the advantages of the two-mesh and duality argument estimators are not as pronounced, which implies that the MMS may have been biasing refinement-based estimators due to the set of nil true derivatives.

In general, we established that the residual source estimator is a viable and attractive spatial discretization error estimator on a wide array of problems for its accuracy, particularly for DGFEM-0, reduced computational cost versus a refinement-based method, and reduced tendency to underestimate the true error. Furthermore, because it directly approximates the error in the angular flux, the error in any quantity computed from the angular flux can be itself directly approximated, unlike norm-based methods, which require heuristic extensions to achieve the same purpose.

Acknowledgements

This material is based upon work supported under a Department of Energy, Office of Nuclear Energy, Integrated University Program Graduate Fellowship. Any opinions, findings, conclusions or recommendations expressed in this publication are those of the authors and do not necessarily reflect the views of the Department of Energy Office of Nuclear Energy. The work is also supported in part by the Department of Energy National Nuclear Security Administration under Award Number *DENA0002576*.

References

References

[1] T. Plewa, T. Linde, V. G. Weirs, Adaptive mesh refinement - theory and applications, in: Proceedings of the Chicago Workshop on Adaptive Mesh Refinement Methods, Chicago, IL, 2003.

[2] J. S. Warsa, A. K. Prinja, p-adaptive numerical methods for particle transport, Transport Theory and Statistical Physics 28 (1999) 229–270.

[3] Y. Wang, J. Ragusa, Application of hp adaptivity to the multigroup diffusion equations, Nuclear Science and Engineering 161 (2009) 22–48.

[4] T. Zhang, N. Feng, A posteriori error analysis of the discontinuous finite element methods for first order hyperbolic problems, Applied Mathematics of Computation 218 (5) (2011) 1752–1764.

[5] C. Cartensen, L. F. Demkowicz, J. Gopalakrishnan, A posteriori error control for dpg methods, SIAM Journal on Numerical Analysis 52 (3) (2014) 1335–1353.

[6] E. Larsen, W. M. Jr., Convergence rates of spatial difference equations for the discrete-ordinates neutron transport equations in slab geometry, Nuclear Science and Engineering 73 (1980) 76–83.

[7] W. Reed, T. Hill, Triangular Mesh Methods for the Neutron Transport Equation, Los Alamos Scientific Laboratory, Technical Report LA-UR-73-479, 1973.

[8] P. Lasaint, P. Raviart, On a finite element method for solving the neutron transport equation, in: C. de Boor (Ed.), Mathematical Aspects of Finite Elements in Partial Differential Equations, Academic Press, 1974, pp. 89–123.

[9] G. R. Richter, An optimal-order error estimate for the discontinuous galerkin method, Mathematics of Computation 50 (181) (1988) 75–88.

[10] Y. Wang, J. C. Ragusa, On the convergence of dgfem applied to the discrete ordinates transport equation for structured and unstructured triangular meshes, Nuclear Science and Engineering 163 (2009) 56–72.

[11] J. Pitkäranta, Estimates for the derivatives of the solution to the weakly singular fredholm integral equations, Journal of Mathematical Analysis 11 (6) (1980) 952–968.

[12] D. Fournier, R. Herbin, R. L. Tellier, Discontinuous galerkin discretization and *hp*-refinement for the resolution of the neutron transport equation, SIAM J. Sci. Comput. 35 (2) (2013) A936–A956.

[13] N. K. Madsen, *A Posteriori* error bounds for numerical solutions of the neutron transport equation, Mathematics of Computation 124 (27) (1973) 773–780.

[14] O. Zienkiewicz, J. Zhu, A simple error estimator and adaptive procedure for practical engineering analysis, International Journal for Numerical Methods in Engineering 24 (1987) 337–357.

[15] O. Zienkiewicz, J. Zhu, The superconvergent patch recovery and *A Posteriori* error estimates. part 1: The recovery technique, International Journal for Numerical Methods in Engineering 33 (1992) 1331–1364.

[16] O. Zienkiewicz, R. Taylor, J. Zhu, The Finite Element Method: Its Basis and Fundamentals, Elsevier Butterworth-Heinemann, Burlington, MA, 2005.

[17] T. Grätsch, K.-J. Bathe, *A Posteriori* error estimation techniques in practical finite element analysis, Computers and Structures 83 (2005) 235–265.

[18] W. L. Oberkampf, C. J. Roy, Verification and Validation in Scientific Computing, Cambridge University Press, Cambridge, UK; New York, 2010.

[19] Y. Wang, J. C. Ragusa, Standard and goal-oriented adaptive mesh refinement applied to radiation transport on 2d unstructured triangular meshes, Journal of Computational and Applied Mathematics 230 (2011) 763–788.

[20] S. O'Brien, Y. Y. Azmy, *A Posteriori* error estimators for the discrete ordinates approximation of the one-speed neutron transport equation, in: International Conference on Mathematics and Computational Methods Applied to Nuclear Science & Engineering (M&C 2013), Sun Valley, Idaho, USA, 2013.

[21] J. C. Ragusa, Y. Wang, A two-mesh adaptive mesh refinement technique for s_n neutral-particle transport using a higher-order dgfem, Journal of Computational and Applied Mathematics 223 (2010) 3178–3188.

[22] J. I. Duo, Y. Y. Azmy, L. T. Zikatanov, A posteriori error estimator and amr for discrete ordinates nodal transport methods, Annals of Nuclear Energy 36 (2009) 268–273.

[23] N. H. Hart, A residual-based *A Posteriori* spatial error estimator for the s_n neutron transport equation, Master's thesis, NC State University (2018).

[24] N. H. Hart, Y. Y. Azmy, J. I. Duo, An *A Posteriori* residual-based spatial discretization error estimator for sn neutron transport, Annals of Nuclear Energy 137.

[25] E. Lewis, W. M. Jr., Computational Methods of Neutron Transport, American Nuclear Society, Inc., La Grange Park, Illinois, 1993.

[26] W. F. Miller, W. H. Reed, Ray-effect mitigation methods for 2-dimensional neutron-transport theory, Nuclear Science and Engineering 62 (3) (1977) 391–411.

[27] X. Hu, Y. Azmy, Asymptotic convergence of the angular discretization error in the scalar flux computed from the particle transport equation with the method of discrete ordinates, Annals of Nuclear Energy 138.

[28] H. V. Jr., On the convergence of the multigroup approximations for multidimensional media, Annali di Matematica Pura ed Applicata 140 (1985) 179–207.

[29] J. I. Duo, Error estimates for nodal and short characteristics spatial approximations of two-dimensional discrete ordinates method, Ph.D. thesis, The Pennsylvania State University, University Park, PA (2008).

[30] S. Schunert, Development of a quantitative decision metric for selecting the most suitable discretization method for s_n transport problems, Ph.D. thesis, North Carolina State University, Raleigh, NC (2013).

[31] Y. Wang, Adaptive mesh refinement solution techniques for the multigroup s_n transport equation using a high-order discontinuous finite element method, Ph.D. thesis, Texas A&M University, College Station, TX (May 2009).

[32] C. Führer, G. Kanschat, *A Posteriori* error control in radiative transfer, Computing 58 (1997) 317–334.

[33] K. Segeth, A review of some *A Posteriori* error estimates for adaptive finite element methods, Mathematics and Computers in Simulation 80 (2010) 1589–1600.

[34] J. Peterson, J. Morel, J. Ragusa, Residual monte carlo for the one-dimensional particle transport equation, SIAM Journal of Scientific Computing 38 (6) (2016) B941–B961.

[35] N. H. Hart, Performance analysis of spatial discretization error estimators for radiation transport discrete ordinates methods, Ph.D. thesis, North Carolina State University, Raleigh, NC (2020).

[36] J. Arkuszewski, J. Mika, T. Kulikowska, Effect of singularities on approximation in sn methods, Nuclear Science and Engineering 49 (1) (1972) 20–+.

[37] in: E. F. Toro (Ed.), Godunov Methods: Theory and Applications, Kluwer Academic/Plenum Publishers, 2001.

[38] Z. Zlatev, I. Dimov, I. Faragó, Ágnes Havasi, The basic properties of richardson extrapolation, in: R. Abgrall, J. A. J. de la Plata, J.-M. Coron, A. S. Fokas (Eds.), Richardson Extrapolation: Practical Aspects and Applications, De Gruyter, 2018, Ch. 1, pp. 1–22.

[39] A. Owens, J. Kophazi, J. Welch, M. Eaton, Energy dependent mesh adaptivity of discontinuous isogeometric discrete ordinate methods with dual weighted residual error estimators, Journal of Computational Physics 335 (2017) 352–386.

[40] E. Lewis, M. Smith, N. Tsoulfanidis, G. Palmiotti, T. Taiwo, R. Blomquist, Benchmark specification for deterministic 2-d/3-d mox fuel assembly transport calculations without spatial homogenization (c5g7 mox), NEA/NSC.

[41] Benchmark on Deterministic Transport Calculations Without Spatial Homogenisation: A 2-D/3-D MOX Fuel Assembly Benchmark, Nuclear Energy Agency Organisation for Economic Co-Operation and Development, Paris, France, 2003.

[42] M. Lei, Y. Peneliau, Y. Song, Analysis of dogleg duct experiments with 14-mev neutron source using tripoli-4 monte carlo transport code, IEEE Transactions on Plasma Science 46 (2018) 1180–1185.

[43] IAEA, Evaluated nuclear data file (endf) (2020).
URL `https://www-nds.iaea.org/exfor/endf.htm`